Energy & Buildings 369 (2026) 117925

Contents lists available at ScienceDirect

Energy & Buildings

journal homepage: www.elsevier.com/locate/enb

Comparative analysis of BTES, ATES, and power-to-hydrogen systems for seasonal storage in public building clusters

Lianghan Cong [a,*], Xiaoshu Lü [a,b,c], Shuaiyi Lu [c], Pan Jiang [c]

[a] Renewable Energy and Built Environment, School of Technology and Innovations, University of Vaasa, P.O.Box 700, FIN-65101 Vaasa, Finland
[b] Department of Civil Engineering, Aalto University, P.O.Box 12100, FIN-02150 Espoo, Finland
[c] Construction Engineering College, Jilin University, Changchun, Jilin, 130026, China

ARTICLE INFO

Keywords:
Seasonal thermal storage
Building energy consumption
Aquifer thermal energy storage
Borehole thermal energy storage
H2 energy

ABSTRACT

This study compares three seasonal storage pathways for 44 public buildings with shared rooftop PV in Drammen, Norway. The buildings face a strong mismatch between summer PV surplus and winter heating demand. The three pathways are borehole thermal energy storage (BTES), aquifer thermal energy storage (ATES), and a electricity-to-hydrogen-to-electricity chain. We use measured hourly data from March 2020 to February 2021. Each pathway absorbs the summer PV surplus, stores it across the season, and returns it during the heating period. BTES and ATES are assessed as thermal storage pathways, while the hydrogen chain is evaluated as an electricity-side storage pathway. BTES injects 10,208 MWh of thermal energy into the ground and recovers 5339 MWh in winter. The seasonal recovery efficiency is close to 52%. ATES at a baseline groundwater velocity of 0.15 m per day recovers 6229 MWh from the same input and reaches 61%, the highest of the three. The hydrogen chain recovers 1452 MWh of electricity from 4455 MWh of summer surplus, giving a round-trip efficiency near 33%. ATES recovery depends strongly on local hydrogeology. Across a sweep of groundwater velocities from 0.02 to 0.30 m per day, recovery ranges from 71% down to 50%. At velocities above 0.25 m per day ATES drops below BTES. Under high-carbon grid conditions, annual avoided emissions reach up to about 85 t CO_2 per building for BTES and 110 t per building for ATES. The hydrogen chain has the highest annualised cost. Per kWh of electricity delivered it is roughly fifteen times that of BTES. BTES remains the robust thermal option when aquifer conditions are unfavourable, while ATES is preferable where hydrogeology permits.

1. Introduction

As the building sector moves toward deep decarbonisation and high penetration of renewable energy, the seasonal imbalance between supply and demand has become a major obstacle for energy systems in northern climates [1]. Winter heating loads in the Nordic region are exceptionally high, while summer provides abundant solar and ambient heat resources. This temporal mismatch keeps fossil fuels embedded in heating systems, even under aggressive renewable expansion strategies [2]. Seasonal Thermal Energy Storage (STES) is therefore increasingly viewed as an essential pathway for achieving high shares of renewable heating and improving building-level self-sufficiency [3]. Established STES technologies include Borehole Thermal Energy Storage (BTES), Aquifer Thermal Energy Storage (ATES), and Pit Thermal Energy Storage (PTES), alongside emerging concepts such as phase-change and thermochemical storage [4].

Recent advances in BTES research focus on borehole field configurations, subsurface thermal conduction, and long-term cycling performance. Case studies and reviews demonstrate that BTES can store large volumes of low-grade heat across seasons, making it one of the most effective options for increasing renewable heat utilisation [5]. Well-known demonstration projects, such as the Drake Landing Solar Community in Okotoks, Alberta (Canada) and the high-temperature BTES system in Mol, Belgium, have confirmed the feasibility and stability of BTES in cold regions [6,7]. BTES performance is strongly governed by soil and bedrock conductivity, borehole spacing, groundwater flow conditions, and storage size, with systems generally reaching stable efficiency only after a thermal acclimation phase [8,9]. In particular, regional groundwater throughflow can drive thermal-plume drift away from the borehole field, reducing recoverable heat in winter; this effect is most pronounced in permeable sedimentary settings and is suppressed in low-permeability crystalline rock such as the Fennoscandian Shield

* Corresponding author.
E-mail address: lianghan.cong@uwasa.fi (L. Cong).

https://doi.org/10.1016/j.enbuild.2026.117925
Received 18 November 2025; Received in revised form 5 July 2026; Accepted 6 July 2026
Available online 7 July 2026
0378-7788/

[9,10].

As an open-loop storage option, ATES has reached large-scale deployment in the Netherlands, Sweden, and other countries, particularly in commercial buildings and district energy networks [11]. It offers high recovery efficiency and favourable costs, yet its performance is highly sensitive to local hydrogeological conditions. Groundwater flow velocity, aquifer thickness, and heterogeneity can drive thermal plume drift, reducing system performance when geological conditions are suboptimal [12,13]. High-temperature ATES may also induce subsurface geochemical alterations, necessitating long-term monitoring and regulation [14]. Despite these constraints, ATES remains highly relevant for buildings requiring both heating and cooling, and recent work continues to explore its potential for cross-season high-temperature storage.

Hydrogen has also emerged as a candidate for seasonal energy storage due to its high energy density and ability to bridge long-duration supply gaps [15–17]. Converting surplus summer photovoltaic electricity into hydrogen and using hydrogen fuel cells (typically proton-exchange-membrane fuel cells, PEMFC) for winter electricity generation is considered a promising option for addressing the seasonal mismatch between renewable electricity supply and heating-driven electricity demand [18–20]. This mismatch is particularly pronounced in high-latitude regions, where summer PV output and winter heating loads are strongly anti-correlated; in temperate climates the seasonal contrast is much weaker, and short-duration storage may suffice [21,22]. Studies in remote microgrids, rail infrastructure, and regional energy systems show that hydrogen storage can enhance self-sufficiency, reduce renewable curtailment, and increase the flexibility of integrated electricity–gas–heat networks [23–25]. However, hydrogen storage typically achieves only 30–40% round-trip efficiency (defined here as the ratio of recovered electrical energy at the fuel cell to the electrical energy initially consumed for electrolysis, after accounting for storage retention losses), and high capital costs and conversion losses continue to limit its competitiveness in most building applications [26].

Despite substantial progress, several knowledge gaps remain. First, cross-technology comparisons of BTES, ATES, and hydrogen storage within the same building cluster remain limited [27,28]. Most existing studies focus on the modelling, optimisation, or techno-economic assessment of individual storage technologies, which restricts their applicability to real-world technology selection. Second, relatively few studies combine hourly building-load profiles, meteorological records, and time-varying electricity prices within a unified seasonal-storage assessment, although intra-day load variability and price fluctuations can substantially influence storage operation and economic performance [29,30]. Third, policy- and future-oriented scenarios, including grid decarbonisation, carbon pricing, and dynamic electricity tariffs, remain insufficiently integrated into seasonal-storage evaluation, creating uncertainty regarding long-term cost and emission outcomes [1]. Fourth, the interaction between building type, demand characteristics, and storage-technology suitability has not been systematically examined, making it difficult to identify which seasonal storage pathway best aligns with specific building-load profiles [31].

This study develops a unified hourly energy-balance and annualised-cost framework to compare BTES, ATES, and a power-to-hydrogen-to-power pathway for 44 public buildings in Drammen, Norway. The framework combines measured energy use, meteorological data, PV generation estimates, electricity prices, storage-pathway models, and carbon-intensity scenarios to evaluate energy recovery, winter import reduction, cost, and emissions. The objective is to provide decision-relevant evidence for seasonal-storage planning in cold-climate public-building clusters.

Section 2 presents the case study, data, framework, models, and indicators; Section 3 reports energy, cost, emission, and sensitivity results; Section 4 discusses technology-selection implications and limitations; and Section 5 concludes the study.

2. Materials and methods

2.1. Case-study buildings and input data

This study focuses on Drammen in southeastern Norway, a high-latitude cold-climate city with strong winter heating demand and substantial electrification of building heat. The analysis uses the COFACTOR Drammen dataset published in Scientific Data [32]. One building is excluded because of missing data, leaving 44 public buildings: 20 kindergartens, 16 schools, 7 nursing homes, and 1 office building. Floor areas range from 188 to 8513 m^2, construction years from 1800 to 2015, and users from 16 to 600 per building. A complete one-year period from March 2020 to February 2021 is selected, covering hourly electricity imports, space heating, domestic hot water, and ventilation loads. Because the buildings share a common urban area and broadly similar geological context, they are treated as a candidate public-building cluster for community-scale seasonal storage.

The dataset also provides hourly meteorological observations and building attributes for model parameterisation and load-pattern analysis. Hourly day-ahead electricity prices from Nord Pool [33] are used to represent Nordic market price signals. The COFACTOR data underwent quality-control procedures, including correction of erroneous values, removal of missing segments, elimination of repeated zeros, and unit harmonisation. Electricity data originate mainly from AMS smart meters. Fig. 1 presents the study region; individual building locations are not shown because of the anonymisation protocol.

2.2. PV baseline and study framework

The assessment framework is designed to compare the three seasonal-storage pathways under the same building-load, PV-surplus, price, and emission assumptions. It proceeds in four steps: constructing the PV baseline, quantifying seasonal mismatch, applying pathway-specific storage models, and evaluating energy, cost, and emission indicators. This sequence keeps the case-study data and comparison logic explicit before the physical storage equations are introduced.

First, hourly PV generation is estimated from each building's available rooftop area and local meteorological data. New PV output is combined with existing PV generation, building electricity demand, and solar-thermal output where available. Solar-thermal production is translated into an equivalent electricity-demand offset using either a heat-pump COP or electric-boiler efficiency. The resulting hourly PV baseline distinguishes direct self-consumption, grid imports, and grid exports.

Second, hourly results are aggregated to daily, monthly, and annual scales to calculate the self-sufficiency ratio (SSR) and self-consumption ratio (SCR) for individual buildings and for the full cluster. Nord Pool day-ahead prices are then applied to imports and exports to construct a price-based economic baseline. Seasonal storage is coupled on top of this PV baseline so that each pathway uses the same summer surplus and is assessed against the same winter demand.

For the BTES pathway, we represent a vertical-borehole field by discretising the one-dimensional heat-conduction equation in cylindrical coordinates over a symmetric unit cell, with the outer boundary placed at the borehole half-spacing as an adiabatic plane [34]. The unit cell is run over six annual cycles to reach a quasi-steady seasonal state. Geometric parameters (borehole radius 0.075 m, spacing 3.8 m, depth 50 m) and ground thermal properties follow the Kvalsvik et al. (2024) [9] Drammen Fjell HT-BTES field. The borehole-wall heat flux is integrated over summer charging, intermediate storage, and winter recovery to obtain the seasonal recovery efficiency.

For the ATES pathway, a lumped thermal-cylinder model is used. Summer-injected heat forms an approximately cylindrical warm volume around the well; seasonal recovery is reduced by conduction across the cylinder boundary, ambient groundwater-flow displacement of the warm volume, and vertical conduction to the confining aquitards

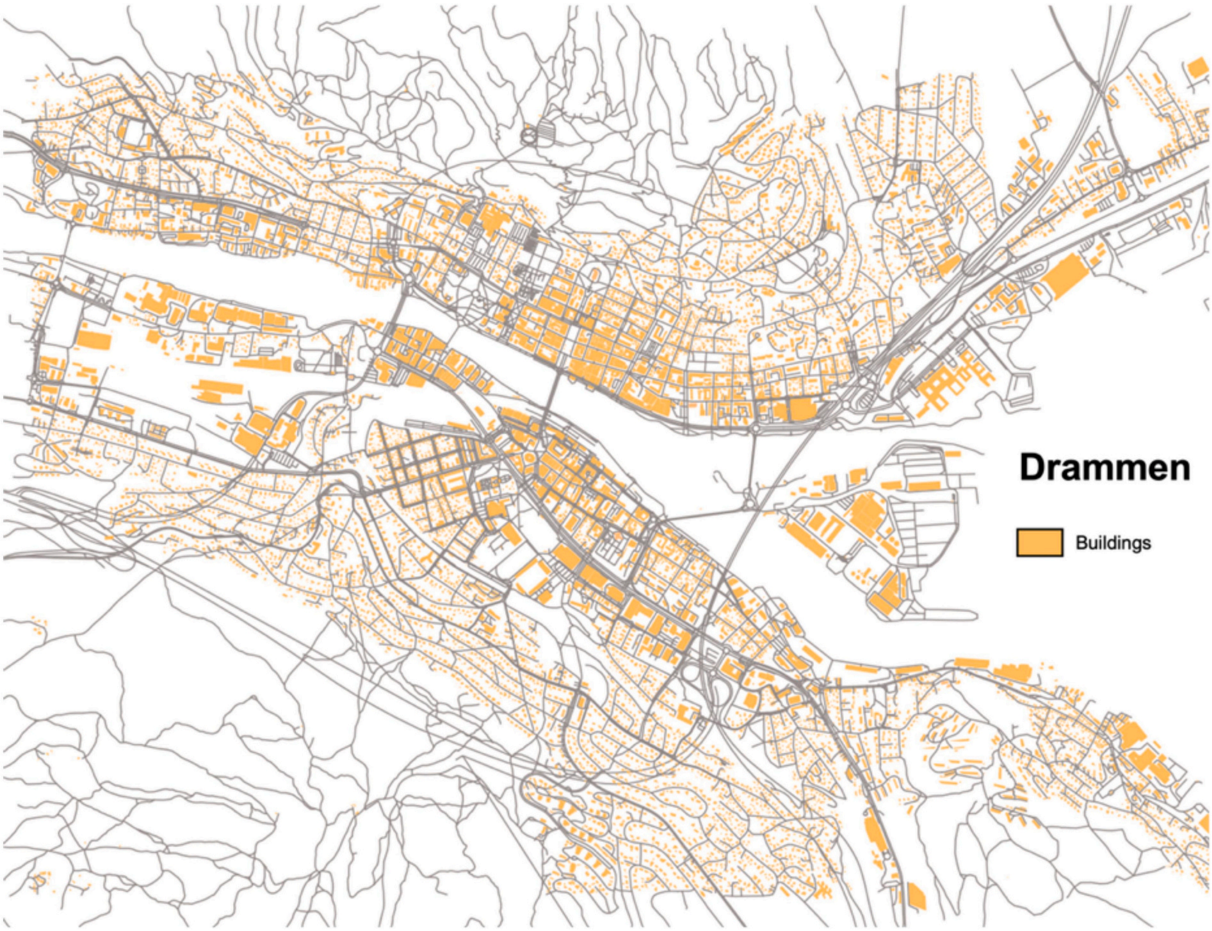

Fig. 1. Urban structure of the study area. Individual building locations are not displayed due to anonymisation requirements.

[35,36]. Given aquifer thickness, injection temperature rise, volumetric heat capacity, thermal diffusivity, and groundwater flow velocity, we estimate the seasonal recovery efficiency and the corresponding monthly electricity offset. Similar to BTES, a time-decreasing discharge COP is applied to capture seasonal variation in monthly electricity offset and cost.

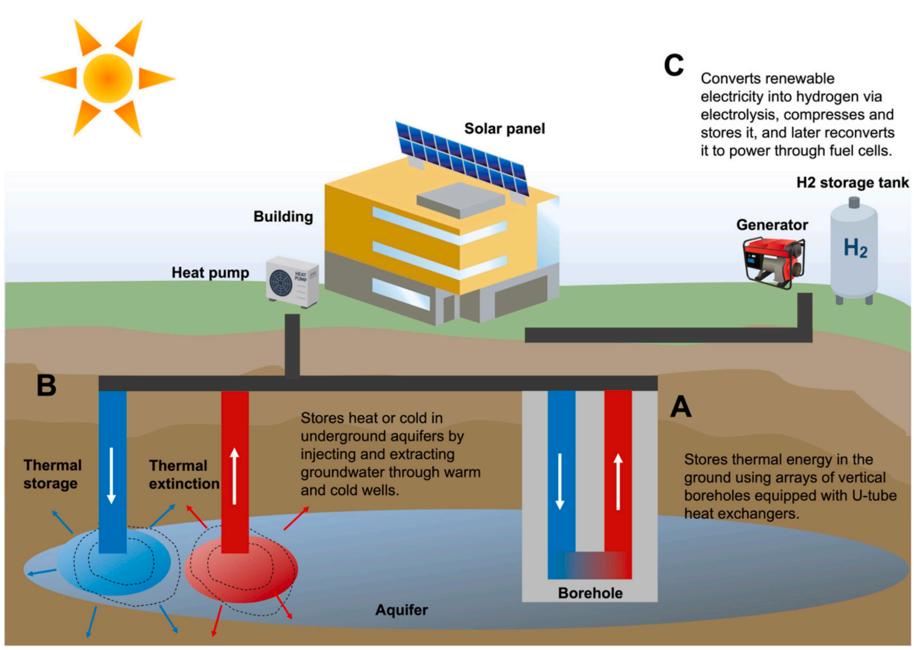

Fig. 2. Framework of the three seasonal storage pathways: A for BTES, B for ATES, and C for hydrogen storage.

For the hydrogen pathway, the model follows an electricity–hydrogen–electricity chain consisting of electrolysis, high-pressure storage, and fuel-cell conversion [16,17,26]. Electrolyser efficiency, storage retention, and fuel-cell efficiency are explicitly included to define the basic round-trip efficiency. Monthly surplus PV electricity in summer determines annual hydrogen production and the rated electrolyser capacity. Winter hydrogen recovery follows a linear monthly decay profile, constrained so that annual discharge does not exceed annual production. After accounting for storage losses, the final recovered electricity and monthly output are obtained and integrated into the electricity balance. The rated fuel-cell capacity and hydrogen storage size are then inferred. Fig. 2 illustrates the framework for the three storage pathways.

Finally, all pathways are evaluated with a unified annualised-cost method. CAPEX and OPEX for PV, BTES, ATES, and hydrogen components are annualised using technology-specific lifetimes and a common discount rate. The annualised costs are compared with baseline electricity costs and storage-driven savings, and the same carbon-intensity scenarios are applied to all three pathways. This produces a consistent basis for technology selection rather than three independent case studies.

2.3. Models and evaluation indicators

2.3.1. Photovoltaic modelling

Because the buildings in the dataset are anonymised, rooftop areas are estimated from heated floor area and occupancy information. The procedure is as follows.

(1) Rooftop-area estimation. Assuming similar floor area on each level, rooftop area is estimated as

$$A_{\mathrm{roof}} = \frac{A_{\mathrm{heated}}}{N_{\mathrm{floors}}} \cdot (1+\delta_{\mathrm{r}}) \tag{1}$$

where A_{heated} is the heated floor area (m^2), N_{floors} the number of floors (a per-building attribute), and δ_{r} a dimensionless correction factor accounting for the roof footprint exceeding the per-storey heated floor area. A value of $\delta_{\mathrm{r}} = 0.10$ is adopted — the roof outline is taken as 10% larger than the simple heated-floor-area / floors quotient. This modest allowance reflects three effects: (i) external-wall structure and unheated ancillary spaces, which lie within the roof outline but are not counted in the heated floor area; (ii) eaves and roof overhangs extending beyond the wall line; and (iii) single-storey ancillary volumes common in public buildings.

(2) PV-installable area. Only part of the roof can carry modules, because of ventilation units, skylights, parapets and maintenance access:

$$A_{\mathrm{PV}} = A_{\mathrm{roof}} \cdot \eta_{\mathrm{usable}} \tag{2}$$

The usable fraction η_{usable} is assigned by building type based on typical rooftop-utilisation ranges reported in PV-potential studies [37,38] and typical Nordic public-building roof configurations: kindergartens 0.60, schools 0.50, nursing homes 0.55, offices 0.50.

(3) Installed capacity. Potential capacity uses an area–power density $P_{\mathrm{d}} = 0.20\ \mathrm{kWp/m^2}$ [39]:

$$P_{\mathrm{PV}} = A_{\mathrm{PV}} \cdot P_{\mathrm{d}} \tag{3}$$

(4) Hourly generation of retrofitted PV. Hourly output of the new PV area $A_{\mathrm{PV,new}}$ is

$$PV_{\mathrm{new}}(t) = \mathrm{GHI}(t) \cdot A_{\mathrm{PV,new}} \cdot \eta_{\mathrm{sys}} \tag{4}$$

where GHI(t) is global horizontal irradiation ($\mathrm{kWh/m^2}$) and $\eta_{\mathrm{sys}} = 0.17$ is the overall system efficiency (module, inverter and wiring losses) [40]. Total generation combines existing and new systems:

$$PV_{\mathrm{total}}(t) = PV_{\mathrm{exist}}(t) + PV_{\mathrm{new}}(t) \tag{5}$$

The photovoltaic-modelling parameters are summarized in Table 1.

2.3.2. Electricity-load construction and solar-thermal offset

Hourly electricity load $L_{\mathrm{elec}}(t)$ is taken from sub-metered end-use data where available, otherwise from total metered imports. Solar-thermal output $Q_{\mathrm{solar,th}}(t)$ is converted into an equivalent electricity offset, depending on whether it serves a heat pump or an electric boiler:

$$ST_{\mathrm{el,offset}}(t) = \frac{Q_{\mathrm{solar,th}}(t)}{\mathrm{COP_{HP}}} \quad (\mathrm{heat-pump\ route}) \tag{6}$$

$$ST_{\mathrm{el,offset}}(t) = \frac{Q_{\mathrm{solar,th}}(t)}{\eta_{\mathrm{boiler}}} \quad (\mathrm{electric-boiler\ route}) \tag{7}$$

with $\mathrm{COP_{HP}} = 3.0$ [41] and $\eta_{\mathrm{boiler}} = 0.95$ [42]. The headline simulation uses the heat-pump route. The effective electrical load $L_{\mathrm{eff}}(t)$ is the building electricity demand remaining after this offset, floored at zero:

$$L_{\mathrm{eff}}(t) = \max\left[0, L_{\mathrm{elec}}(t) - ST_{\mathrm{el,offset}}(t)\right] \tag{8}$$

The baseline hourly energy balance is then

$$\mathrm{SelfUse}(t) = \min\left[PV_{\mathrm{total}}(t), L_{\mathrm{eff}}(t)\right] \tag{9}$$

$$\mathrm{Export}(t) = \max\left[0, PV_{\mathrm{total}}(t) - L_{\mathrm{eff}}(t)\right] \tag{10}$$

$$\mathrm{Import}(t) = \max\left[0, L_{\mathrm{eff}}(t) - PV_{\mathrm{total}}(t)\right] \tag{11}$$

with hourly cost and revenue

$$C_{\mathrm{imp}}(t) = \mathrm{Import}(t) \cdot p_{\mathrm{imp}}(t) \tag{12}$$

$$R_{\mathrm{exp}}(t) = \mathrm{Export}(t) \cdot p_{\mathrm{exp}}(t) \tag{13}$$

where p_{imp} and p_{exp} are hourly Nord Pool import and export prices (EUR/kWh). The annual baseline net cost is

$$C_{\mathrm{base}} = \sum_{\mathrm{t}} C_{\mathrm{imp}}(t) - \sum_{\mathrm{t}} R_{\mathrm{exp}}(t) \tag{14}$$

The load-construction and solar-thermal-offset parameters are summarized in Table 2.

2.3.3. Daily and annual indicators

The match between PV generation and demand is characterised by the self-sufficiency ratio (SSR) and self-consumption ratio (SCR), computed at daily, monthly and annual resolution:

$$\mathrm{SSR_d} = 1 - \frac{Import_{\mathrm{d}}}{L_{\mathrm{elec,d}}} \tag{15}$$

Table 1
Photovoltaic-modelling parameters.

Symbol	Parameter	Value	Source
δ_{r}	Rooftop correction factor (Eq. 1)	0.10	Verified against building data (reproduces installable PV areas)
η_{usable}	Usable roof fraction by type (Eq. 2)	0.50–0.60	Assumed by building category
P_{d}	Area–power density (Eq. 3)	0.20 $\mathrm{kWp/m^2}$	[39]
η_{sys}	PV system efficiency (Eq. 4)	0.17	[40]

Table 2
Load and solar-thermal-offset parameters.

Symbol	Parameter	Value	Source
COP_{HP}	Heat-pump COP for solar-thermal offset (Eq. 6)	3.0	Nordic ground-source HP [41]
η_{boiler}	Electric-boiler efficiency (Eq. 7)	0.95	[42]
Offset route	Solar-thermal use in headline run	Heat-pump route (Eq. 6)	Model setting

$$SCR_d = \frac{SelfUse_d}{PV_{total,d}} \tag{16}$$

Annual SSR and SCR are obtained the same way from annual sums. SSR is reported against L_{elec} (the gross electrical load) so that the indicator is comparable across buildings regardless of solar-thermal contribution.

2.3.4. Heat-pump COP

Two COP treatments are implemented. The headline results use a constant-COP setting: a charging-side COP of 3.0 for summer heat injection and a base discharging-side COP of 2.5 for winter heat recovery. A temperature-dependent Carnot form is retained as an alternative used only in the COP sensitivity tests:

$$COP_{base} = \eta_{HP,sys} \cdot \frac{T_h}{T_h - T_c} \tag{17}$$

where T_h and T_c are sink and source temperatures (K), and $\eta_{HP,sys} = 0.45$ is the overall system-efficiency factor relative to the Carnot limit [43]. A heat-exchanger temperature difference $HEX_{DT} = 3^{\circ}C$ and network-loss factor $PIPE_{EFF} = 0.97$ are applied [44].

During winter discharge, reservoir temperatures fall as heat is withdrawn; the discharge-side COP is therefore reduced month by month:

$$COP_{dis}(m) = COP_{base} \cdot (1 - \delta_c)^{m-1} \tag{18}$$

where δ_C is the monthly COP-degradation rate, set to 0.06 for BTES and 0.04 for ATES, with a COP floor of 1.6 (BTES) and 1.7 (ATES) to avoid unphysical values. The winter (discharge) months are November, December, January and February; May–September are the summer charging months and October is treated as an inter-seasonal transition.

The heat-pump COP parameters used in the headline and sensitivity cases are summarized in Table 3.

2.3.5. Seasonal-storage pathways and physical models

Three storage pathways are compared under the same PV-surplus and winter-demand boundary conditions (Table 4). BTES and ATES are thermal pathways: summer surplus electricity is converted to heat for seasonal storage and recovered heat offsets winter electricity demand through the discharge-side COP. The hydrogen pathway is an electrical route in which surplus electricity is converted to hydrogen and later reconverted to electricity. The reduced-order model for each pathway is described below, followed by its parameter table.

Table 4
Seasonal-storage pathways used in this study.

Pathway	System type	Dominant mechanism
A	BTES	Radial heat conduction in the ground around a borehole
B	H_2	Electrochemical conversion and storage
C	ATES	Heat storage in a saturated aquifer with conduction and ambient-groundwater-flow displacement losses

(1) Pathway A - BTES

Heat is stored by radial conduction in the ground around a vertical borehole. The temperature field is governed by the 1-D heat-conduction equation in cylindrical coordinates:

$$\frac{\partial T}{\partial t} = \alpha\left(\frac{\partial^2 T}{\partial r^2} + \frac{1}{r}\frac{\partial T}{\partial r}\right) \tag{19}$$

where r is radial distance (m), α the ground thermal diffusivity (m^2/s) and T temperature. The boundary conditions are:

- Inner boundary at the borehole wall: $T(r_b, t) = T_{in}$ during charging — i.e. the condition is imposed at the borehole-wall radius r_b, not at $r = 0$;
- •Outer boundary: a zero-flux (adiabatic) condition at $r = R_{field}$, the borehole half-spacing. This represents the symmetry plane mid-way between neighbouring boreholes in a densely packed field, so that the single-borehole cell approximates the mutual thermal screening of the full field.

The equation is solved with an explicit finite-difference scheme over multiple annual cycles until a quasi-steady seasonal cycle is reached, subject to the stability condition

$$\Delta t \le \frac{\Delta r^2}{4\alpha} \tag{20}$$

Borehole-wall heat flux $q(t)$ is obtained from the near-wall temperature gradient and the ground thermal conductivity. Seasonal charging energy integrates the wall flux over the borehole length L:

$$E_{in} = \int q(t) \cdot 2\pi r_b L \, dt \tag{21}$$

with $L = 50$ m (the borehole depth at the Fjell Primary School field used for parameterisation). The recovery efficiency is

$$\eta_A = \frac{E_{out}}{E_{in}} \cdot TopLossFactor \tag{22}$$

with $TopLossFactor = 0.90$, representing conductive losses through the top and bottom of the storage volume. Because L cancels in the efficiency ratio Eout/Ein, the recovery efficiency is independent of the assumed borehole depth in this reduced-order representation. Geological and

Table 3
Heat-pump COP parameters.

Symbol	Parameter	Value	Source
Charging COP	Summer heat-injection COP (headline run)	3.0	Constant-COP setting; Nordic GSHP
Discharge COP (base)	Winter heat-recovery base COP (headline run)	2.5	Constant-COP setting
$\eta_{HP,sys}$	Carnot system-efficiency factor (Eq. 17)	0.45	[43]; used in sensitivity mode only
$HEX_{\Delta T}$	Heat-exchanger ΔT (Eq. 17)	3°C	[44]
$PIPE_{EFF}$	Network-loss factor	0.97	[44]
δ_C	Monthly COP-degradation rate (Eq. 18)	0.06 (BTES); 0.04 (ATES)	Reservoir-cooling representation
COP floor	Minimum discharge COP	1.6 (BTES); 1.7 (ATES)	Numerical bound
Winter months	Discharge season	Nov, Dec, Jan, Feb	Heating-demand peak

geometric parameters follow the Fjell Primary School HT-BTES field in Drammen [9], which is used as a field-scale analogue with comparable geology and borehole layout. The headline calculation sets $\eta_A = 0.523$ from the field-informed parameterisation [9], and Eqs. (19)–(22) are retained for the sensitivity analysis in Section 3.7. The per-building borehole count is sized from each building's summer surplus and seasonal heat demand. This model represents the main radial-conduction storage process and should not be interpreted as a full design model for all three-dimensional borefield effects.

Heat-to-electricity equivalence on the demand side is

$$E_{heat} = E_{export,el} \cdot COP_{charge} \cdot \eta_A \cdot PIPE_{EFF} \tag{23}$$

$$E_{offset,el} = \frac{E_{heat}}{COP_{discharge}} \tag{24}$$

The 1-D radial-conduction approach for BTES follows established analytical and numerical single-borehole formulations [45].

The BTES physical and numerical parameters are listed in Table 5.

(2) Pathway B - Electricity–Hydrogen–Electricity chain

Summer PV surplus is converted to hydrogen by electrolysis, stored under pressure, and reconverted to electricity by a fuel cell in winter. This pathway is therefore evaluated as a power-to-hydrogen-to-power chain rather than as a direct heat-storage technology. The base seasonal round-trip efficiency is defined as recovered fuel-cell electricity divided by electricity consumed for electrolysis, after storage retention losses:

$$\eta_B = \eta_{elec\to H_2} \cdot \eta_{store} \cdot \eta_{H_2\to elec} \tag{25}$$

with $\eta_{elec\to H_2} = 0.80$ (PEM electrolyser, LHV basis), $\eta_{store} = 0.85$ (compression, transfer and leakage retention) and $\eta_{H2\to elec} = 0.60$ (PEM fuel-cell system). This gives a base round-trip efficiency of $\eta_B \approx 0.408$, within the 30–40% range reported for PEM-based power-to-power systems [46].

In addition, recovered hydrogen is subject to a linear monthly decay across the winter discharge season: the recoverable amount in discharge month m is scaled by $(1 - r \cdot (m - 1))$, where the per-building decay rate r is drawn once from the range [0.05, 0.10] using a fixed random seed for reproducibility. Annual recovery is capped so that it cannot exceed annual production. Winter recoverable electricity is

$$E_{elec,B} = E_{export,el} \cdot \eta_B \quad \text{(before monthly decay)} \tag{26}$$

Component sizing. A design margin covers load fluctuation, uneven utilisation and maintenance: electrolyser power = summer-average electrolyser load × 1.2; fuel-cell power = winter-average discharge power × 1.5. Hydrogen-storage capacity is

$$E_{H_2,store} = E_{export,el} \cdot \eta_{elec\to H_2} \cdot \eta_{store} \tag{27}$$

and the corresponding hydrogen mass is

$$m_{H_2} = \frac{E_{H_2,store}}{LHV_{H_2}} \tag{28}$$

with $LHV_{H_2} = 33.33$ kWh/kg (lower heating value of hydrogen, 120 MJ/kg). The representation is a simplified seasonal-chain model intended for comparative assessment; it does not resolve part-load electrolyser operation, fuel-cell degradation, or detailed compression balance-of-plant electricity beyond the lumped storage-retention factor. Electricity-hydrogen-electricity chains for seasonal storage are well documented in microgrid, building, and regional-energy studies [16,26].

The electricity-hydrogen-electricity chain parameters are listed in Table 6.

(3) Pathway C - ATES

The ATES system is modelled as a single warm-well store in a confined aquifer. The cold well is assumed hydraulically and thermally separate and is not represented; multi-well and branched layouts are outside the scope of this reduced-order comparison. To avoid confusion, the ambient groundwater-flow velocity is denoted as v_{gw} throughout this study. It represents the prescribed regional groundwater-flow velocity used to estimate displacement of the warm storage volume during the storage period, rather than a separately derived thermal-front velocity.

Summer injection of seasonal thermal energy E_{inj} into a confined aquifer of thickness H forms an approximately cylindrical warm volume around the well. Its thermal volume and radius are

$$V_{th} = \frac{E_{inj}}{C_{aq} \cdot \Delta T_{inj}} \tag{29}$$

$$R_{th} = \sqrt{\frac{V_{th}}{\pi H}} \tag{30}$$

where C_{aq} is the volumetric heat capacity of the saturated aquifer and ΔT_{inj} the injection temperature rise above ambient. During the storage period three loss mechanisms reduce the recoverable fraction.

- Conduction loss across the cylinder boundary, scaling with the conductive penetration length $\sqrt{\alpha_{aq}\, t_{store}}$ relative to R_{th}:

$$\eta_{cond} = \frac{R_{th}}{R_{th} + \beta_{cond}\sqrt{\alpha_{aq}\, t_{store}}} \tag{31}$$

Ambient-flow displacement loss: regional groundwater flow displaces the warm cylinder by $L_{drift} = v_{gw} \cdot t_{store}$. Recovery from the original well location captures only the geometric overlap of the displaced and original cylinders, represented as the exact area-overlap fraction of two equal circles of radius R_{th} whose centres are L_{drift} apart.

$$\eta_{drift} = \frac{2}{\pi}\left[\arccos(x) - x\sqrt{1 - x^2}\,\right], \quad x = \frac{L_{drift}}{2R_{th}} \tag{32}$$

- Vertical conduction loss to the confining aquitards (clay caps), applied as a constant factor $\eta_{vert} = 0.85$.

The seasonal recovery efficiency of ATES is the product of the three

Table 5
BTES physical and numerical parameters (Pathway A).

Symbol	Parameter	Value	Source
ρ_g	Ground density	2580 kg/m^3	[9]
$c_{p,g}$	Ground specific heat	900 J/(kg·K)	[9]
λ_g	Ground thermal conductivity	3.7 W/(m·K)	[9], from TRT
α	Ground thermal diffusivity	1.59 × 10^{-6} m^2/s	Derived: λ / ($\rho \cdot c_p$)
r_b	Borehole radius	0.075 m	Standard borehole
Spacing	Borehole spacing	3.8 m	[9]
R_{field}	Symmetric-cell outer radius (= half-spacing)	1.9 m	Dense-field symmetry boundary
L	Borehole length (depth)	50 m	Fjell field; cancels in η ratio
Δr	Radial grid spacing	0.05 m	Numerical
Δt	Time step	300 s	Numerical; satisfies Eq. (20)
n_{cycles}	Annual cycles to quasi-steady state	6	Numerical
TopLossFactor	Top/bottom conduction-loss factor (Eq. 22)	0.90	Storage-geometry estimate
η_A	round-trip efficiency	0.523	Calculated from Kvalsvik et al. (2024) [9] field data

Table 6
Electricity–hydrogen–electricity chain parameters (Pathway B).

Symbol	Parameter	Value	Source
$\eta_{elec\to H2}$	PEM electrolyser efficiency (LHV)	0.80	[46,47]
η_{store}	Storage retention (compression, leakage)	0.85	[48]
$\eta_{H2\to elec}$	PEM fuel-cell system efficiency	0.60	[46]
η_B	Base round-trip efficiency	0.408	–
r	Per-building monthly decay rate of recovered H_2	0.05–0.10	Drawn per building, fixed seed
LHV_{H2}	Lower heating value of hydrogen	33.33 kWh/kg	Standard (120 MJ/kg)
EL margin	Electrolyser power design margin	× 1.2	[47]
FC margin	Fuel-cell power design margin	× 1.5	[47]

terms:

$$\eta_C = \eta_{cond}\cdot\eta_{drift}\cdot\eta_{vert} \tag{33}$$

Recoverable heat is then converted to a demand-side electricity offset using the discharge-side COP, exactly as in Eqs. (23)–(24) for BTES:

$$E_{offset,el} = \frac{E_{heat}}{COP_{discharge}}, \quad E_{heat} = E_{inj}\cdot\eta_C \tag{34}$$

This lumped formulation follows the analytical loss framework for ATES recovery efficiency, including conduction, dispersion, and displacement by ambient groundwater flow, set out by Bloemendal and Hartog (2018) [36] and Doughty et al. (1982) [35]. The site is assumed to be underlain by a confined sand-gravel aquifer. We adopt $v_{gw} = 0.15$ m/day as a baseline ambient groundwater-flow velocity for this setting and sweep v_{gw} over 0.02–0.30 m/day to characterise the sensitivity of ATES performance to hydrogeology.

The ATES physical parameters are listed in Table 7.

ATES round-trip efficiency: for ATES, as for BTES, the recovery efficiency η_C is the seasonal round-trip efficiency on the thermal side.

2.3.6. *Techno-economic and emission evaluation*

All pathways are evaluated with a unified annualised-cost method. The capital-recovery factor for discount rate r and technology lifetime n is

$$CRF = \frac{r(1+r)^n}{(1+r)^n - 1} \tag{35}$$

and the annualised cost of a component is

$$\text{Annualised} = CAPEX\cdot CRF + CAPEX\cdot OPEX_{frac} \tag{36}$$

A common discount rate $r = 0.07$ is used for all technologies. The component CAPEX, OPEX fraction and lifetime values are listed in Table 8. Storage CAPEX is applied on a delivered-energy basis (the inventory-based unit cost is converted using the route efficiency).

Net cost and savings. For each pathway the annual net cost is

$$NetCost_{A,B,C} = C_{base} + C_{PV,ann} + C_{route,ann} - Savings \tag{37}$$

where: $C_{PV,ann}$ is the annualised cost of the retrofitted PV system (new PV CAPEX and OPEX, annualised by Eqs. 35–36 with the PV lifetime); and $C_{route,ann}$ is the annualised cost of all storage-route components — for BTES/ATES the storage CAPEX and OPEX, and for H_2 the sum of electrolyser, fuel-cell and hydrogen-storage CAPEX and OPEX. Savings is the reduction in net electricity purchases achieved by seasonal shifting. C_{base} is the baseline net cost of Eq. (14).

Key indicators. Levelised cost of stored energy:

$$LCOE_B = \frac{C_{B,ann}}{E_{elec,B}} \tag{38}$$

$$LCOH_{A/C} = \frac{C_{A/C,ann}}{E_{heat}} \tag{39}$$

and the net benefit of each pathway relative to the baseline,

$$\Delta_{A/B/C} = C_{base} - NetCost_{A/B/C} \tag{40}$$

Operational strategy. A "local-first" dispatch is adopted: summer PV electricity first serves building loads; the remainder drives BTES/ATES charging or hydrogen production; only the final surplus is exported. In winter, storage output serves building demand first and the grid supplies the residual.

3. Results

3.1. *PV baseline performance*

This subsection establishes the seasonal mismatch that motivates the storage comparison. Fig. 3 shows electricity use across the 44 buildings from March 2020 to February 2021, using representative days to avoid excessive hourly-plot density. The building group shows a clear low-summer/high-winter profile: per-building monthly mean consumption is about 6–15 MWh in spring and summer, then rises to about 25–45 MWh in winter, with the highest-consumption buildings exceeding 100 MWh. The December–January peaks define the main winter compensation target. Fig. 4 presents the maximum, minimum, and average electricity consumption across the group.

Using hourly climate data from March 2020 to February 2021, two baseline scenarios are constructed: a no-PV scenario and a scenario with additional rooftop PV. Seasonal storage is then coupled to the PV baseline, because the central question is how summer PV surplus can be

Table 7
ATES physical parameters (Pathway C).

Symbol	Parameter	Value	Source
H	Confined aquifer thickness	20 m	Deep sand–gravel layer; typical LT-ATES screen
ΔT_{inj}	Injection temperature rise above ambient	15 K	Low-temperature ATES; [36]
C_{aq}	Volumetric heat capacity, saturated aquifer	2.8×10^6 J/(m^3·K)	Saturated sand–gravel
α_{aq}	Aquifer thermal diffusivity	0.10 m^2/day	Saturated sand–gravel
β_{cond}	Conduction-loss scaling constant (Eq. 31)	2.0	Analytical loss model
η_{vert}	Vertical conduction-loss factor (aquitards)	0.85	Confining clay caps
$\boldsymbol{v_{gw}}$	Ambient groundwater-flow velocity — baseline	0.15 m/day	Neutral mid-range value
$\boldsymbol{v_{gw}}$	Ambient groundwater-flow velocity — sweep range	0.02, 0.05, 0.10, 0.15, 0.20, 0.30 m/day	Reported as a core result
INJ months	Summer charging season	May–Sep	PV surplus period
EXT months	Winter discharge season	Nov, Dec, Jan, Feb	Heating-demand peak

Table 8
Techno-economic parameters: discount rate, CAPEX, OPEX fraction and lifetime for each component.

Component	CAPEX	OPEX fraction	Lifetime	Source / basis
Discount rate r	0.07 (all technologies)	–	–	Standard rate for public-sector energy projects, consistent with NREL ATB (6.14–7%) and IRENA cost benchmarks [46,49]
PV (retrofit)	200 €/m^2	0.015	25 yr	Rooftop PV system cost from Fraunhofer ISE Photovoltaics Report [50]
BTES	1.90 €/kWh$_{th}$ (inventory)	0.01	30 yr	Borehole-field investment range (0.4–4 €/kWhth) per [11,51]
ATES	3.00 €/kWh$_{th}$ (inventory)	0.01	30 yr	Well + heat-exchanger LT-ATES techno-economic data [28]
H_2 electrolyser	1800 €/kW	0.03	15 yr	PEM electrolyser installed cost [46,52]
H_2 fuel cell	1300 €/kW	0.03	12 yr	PEM fuel-cell system cost [53]
H_2 storage	12 €/kWh$_{H2}$	0.02	20 yr	Pressurised H_2 storage (200–700 bar) [48]

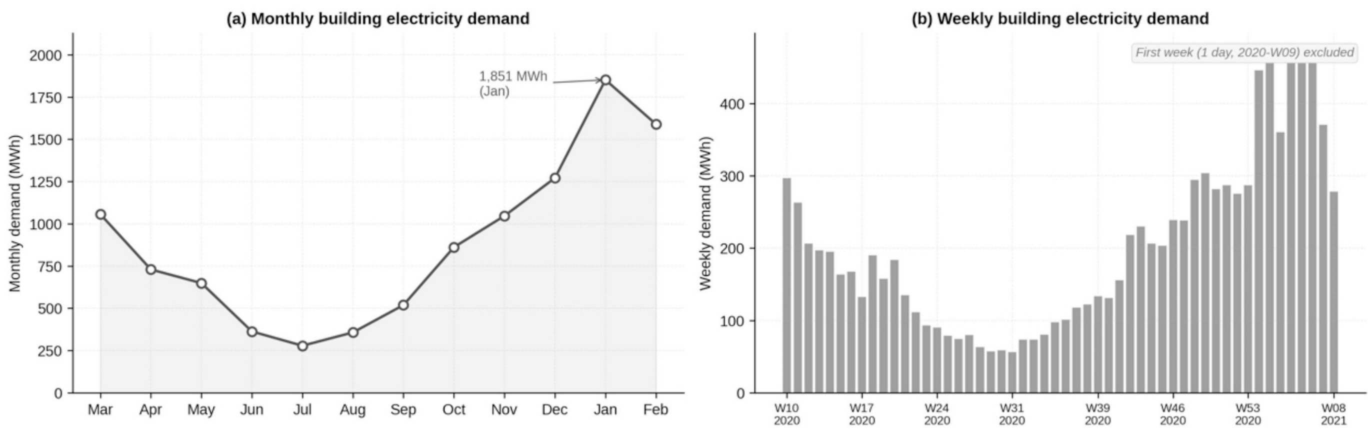

Fig. 3. Building energy demand. (a) Monthly representative-day demand; (b) Weekly demand, starting from week 9 of 2020, with week numbering continuing into 2021.

shifted into the winter heating period.

Monthly self-sufficiency (SSR-m) and self-consumption (SCR-m) under the PV baseline show the expected seasonal contrast (Fig. 5). In summer, SSR-m reaches 0.57–0.68, while SCR-m is low because demand is much lower than PV output. In winter, nearly all PV is self-consumed but absolute generation is small, and SSR-m falls to about 0.02 in December. This confirms that PV alone cannot address the winter demand peak.

Fig. 6 presents the monthly energy balance under the PV baseline. Electricity demand is lowest in summer (280–360 MWh/month for the building group) and peaks in December and January (around 1270–1850 MWh/month). PV generation exhibits strong seasonal variation, reaching 915–1190 MWh/month in summer and nearly zero in winter. PV self-consumption remains roughly 200–250 MWh/month through the summer (because summer demand is far below summer PV), but drops in winter. PV export is highest in summer (700–850 MWh/month) and zero in winter, while electricity imports follow the opposite trend.

3.2. Storage performance: import reduction and energy recovery

The storage comparison first considers how effectively each pathway shifts summer surplus into the winter demand period. Fig. 7 compares monthly electricity imports under the three seasonal-storage pathways with the PV and no-PV baselines. Seasonal storage has little effect on summer imports, which are already low under the PV baseline, but it substantially reduces winter imports.

Under the PV baseline (Import-PV), summer electricity imports drop to 115–270 MWh/month, while winter imports rise sharply above 1250 MWh in December and January. In contrast, the no-PV scenario (Import-NoPV) shows even higher imports year-round, with winter peaks close to 1850 MWh, confirming PV's strong role in reducing summer grid demand.

BTES provides the strongest winter compensation in November, when its import reduction reaches approx. 590 MWh. Across the rest of winter, BTES reductions decrease to approx. 300–440 MWh/month (Dec–Feb). ATES is consistently competitive: it slightly trails BTES in November (around 480 MWh) but outperforms BTES in December (around 590 MWh) and matches it in January and February (300–500 MWh). The hydrogen pathway provides the smallest reduction across all winter months (260–315 MWh) due to its lower round-trip efficiency.

All three pathways behave identically in summer, confirming that summer operations are dominated by PV surplus rather than storage performance. Overall, the thermal pathways deliver the largest winter reductions in grid dependence. Heating-season grid imports (November–March) fall by 31% under ATES, 28% under BTES and 19% under H_2. ATES leads in every mid-winter month with reductions of 47%, 28% and 25% in December, January and February, while H_2 remains noticeably lower throughout.

Fig. 8 presents the monthly self-sufficiency ratio (SSR-m) under the three pathways. All technologies show similar performance in summer, with SSR-m reaching 0.59–0.68 in May–July, comparable to the PV-only scenario. The pathways begin to diverge in winter.

BTES raises SSR-m to about 0.64 in November and remains above the PV baseline through winter, although compensation decreases as the store cools. Hydrogen provides smaller but smoother improvements because of its imposed monthly discharge schedule. ATES gives the smoothest winter profile and remains comparable to or above BTES across most mid-winter months under the baseline groundwater-flow assumption.

Fig. 9 and Fig. 10 show why the three pathways produce different winter outcomes. In the BTES pathway, surplus summer PV electricity is

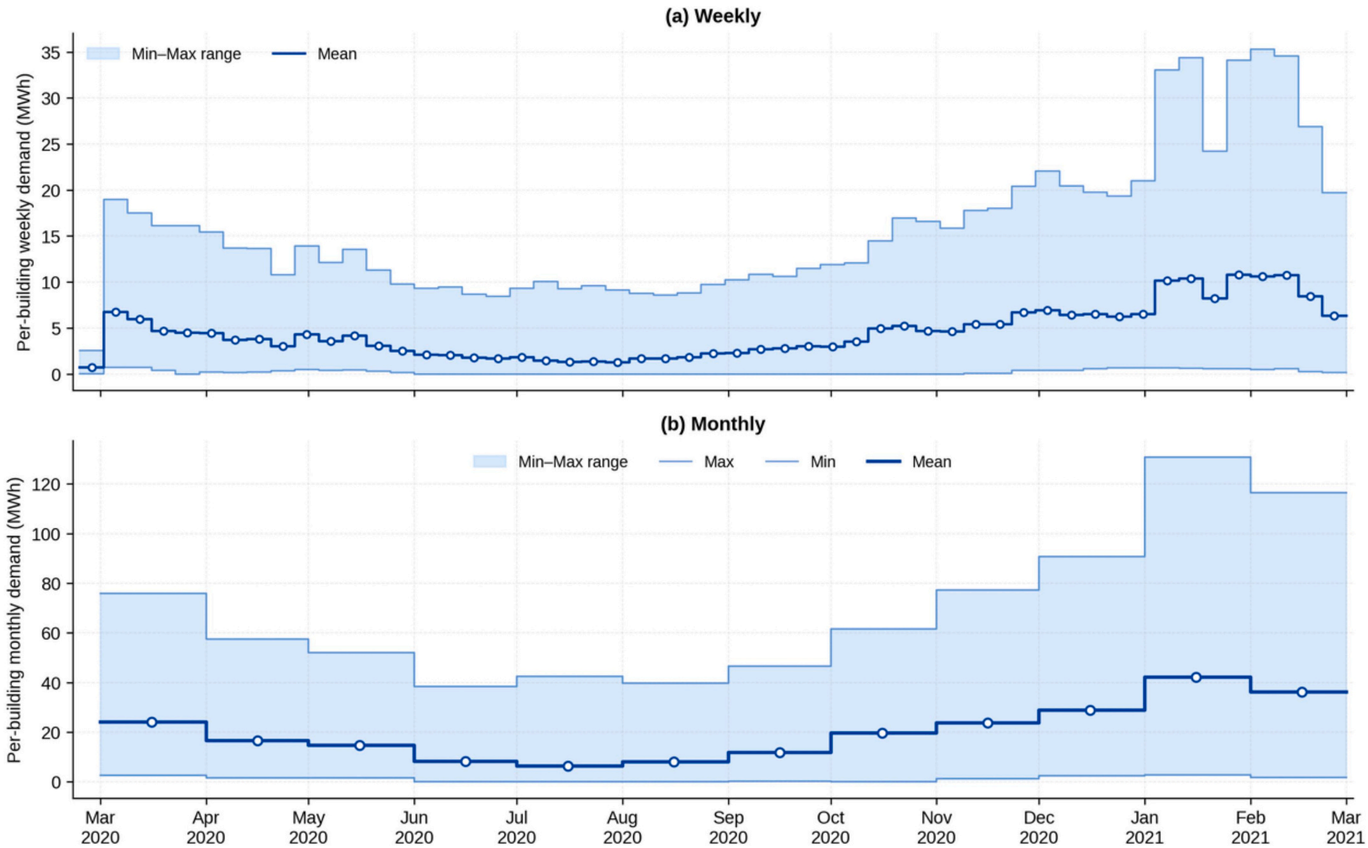

Fig. 4. Maximum, minimum, and average electricity consumption across the building group.

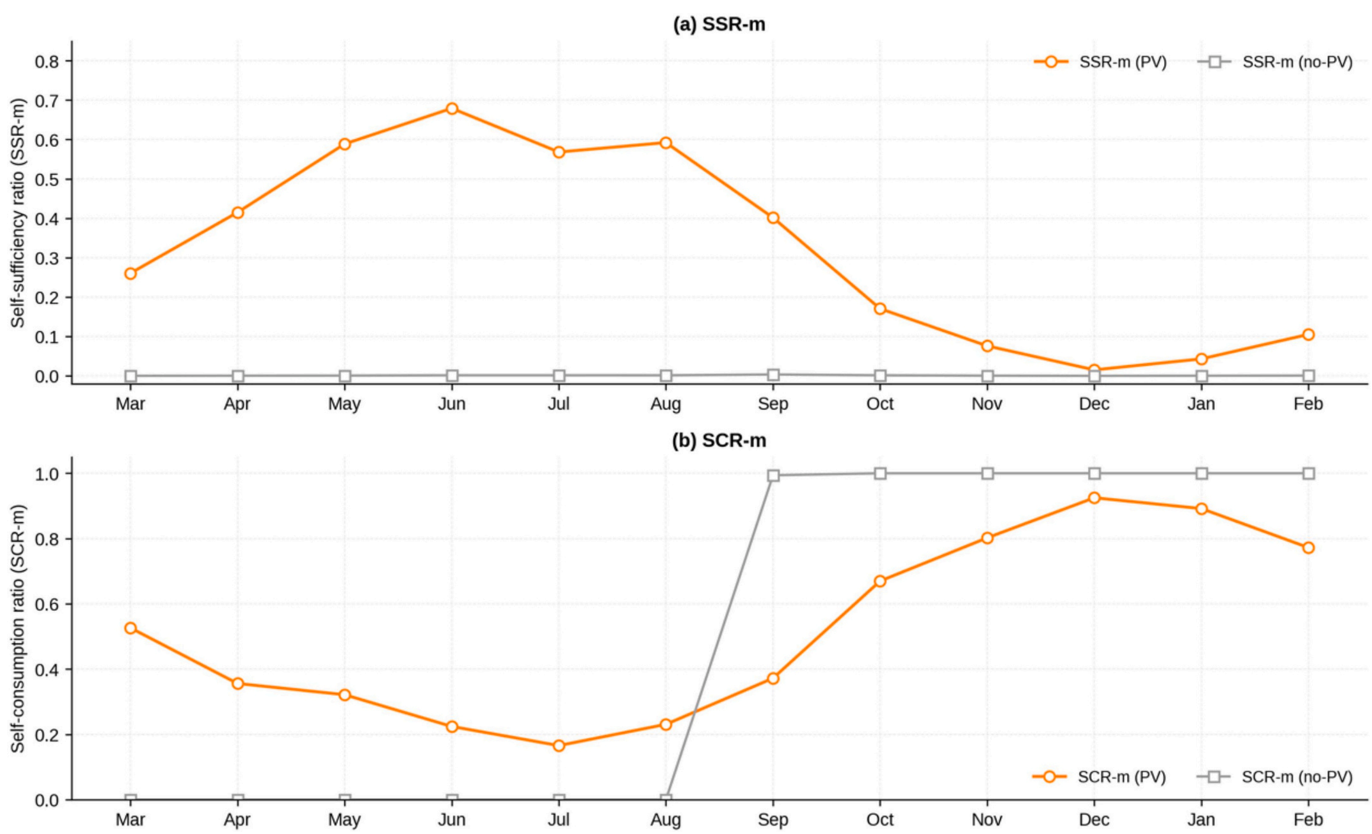

Fig. 5. Monthly self-sufficiency and self-consumption under PV and no-PV baselines.

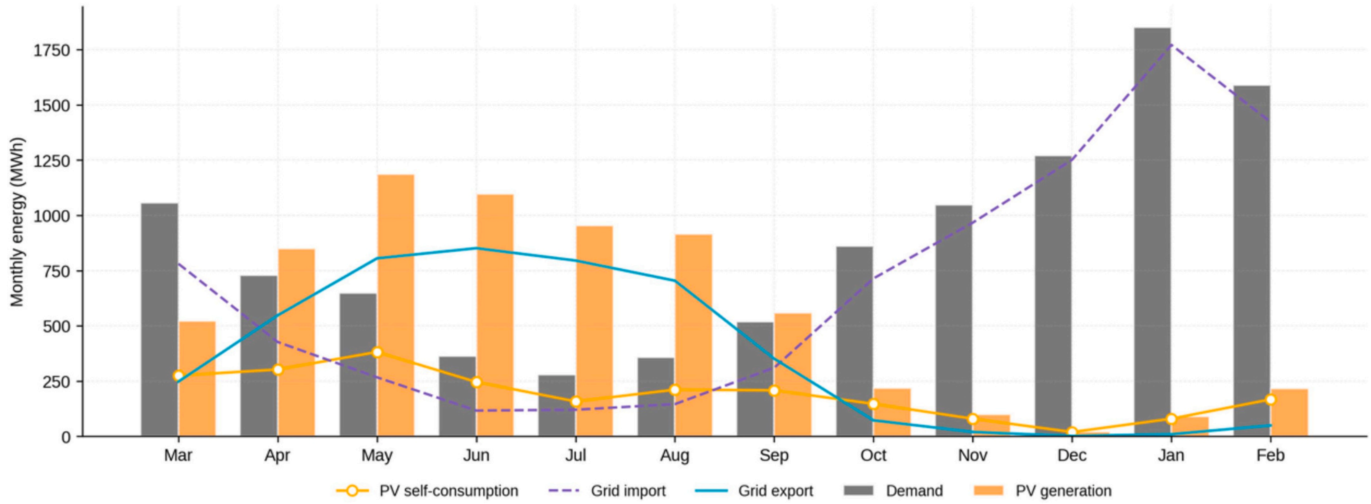

Fig. 6. Monthly electricity demand, PV generation, self-consumption, imports, and exports under the PV baseline.

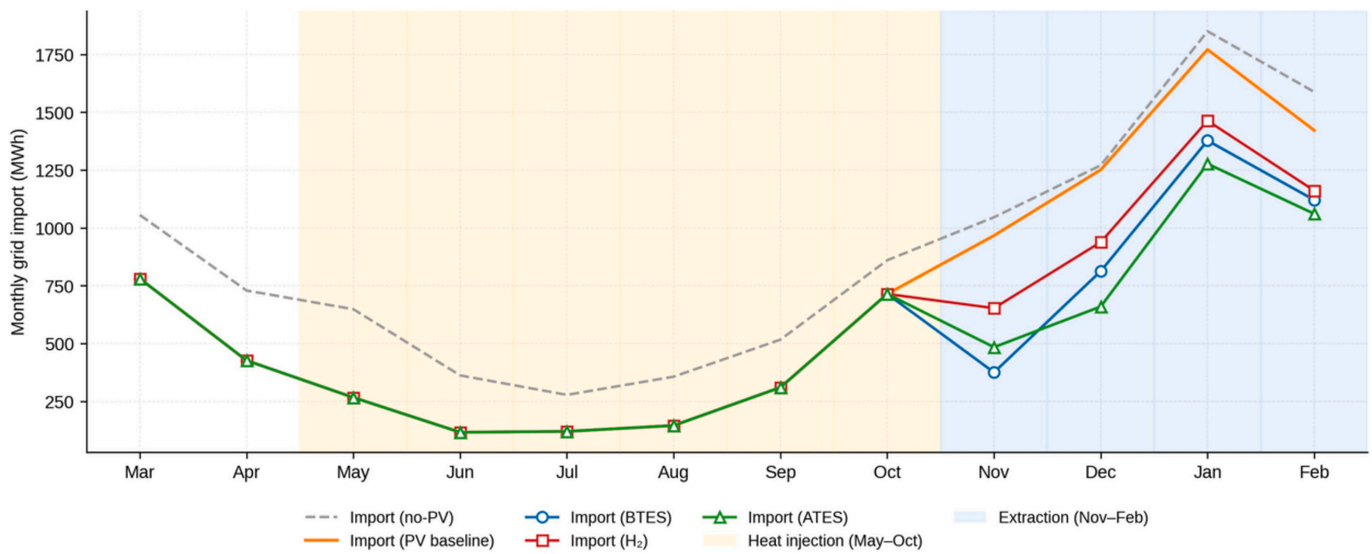

Fig. 7. Monthly electricity imports under the three seasonal storage pathways.

converted into heat through heat pumps, delivering approximately 10,208 MWh of thermal energy into the ground. Seasonal radial conduction losses reduce the recoverable winter heat to 5339 MWh, corresponding to a seasonal round-trip efficiency of about 52%. This pattern can be characterised as high charging, moderate loss, and substantial recovery. It provides strong winter heat compensation, particularly where ATES is not feasible because suitable aquifer conditions are absent.

The H_2 pathway shows a moderate input scale. About 4455 MWh of electricity is used for hydrogen production. Due to conversion losses in electrolysis, compression and storage, and fuel-cell generation, only about 1452 MWh is recovered as electricity, reflecting a round-trip efficiency of roughly 33%. The Sankey diagram shows that losses are distributed across multiple stages of the energy chain.

The ATES pathway absorbs the same 10,208 MWh of summer PV heat as BTES. Under the baseline ambient groundwater-flow velocity $v_{gw} = 0.15$ m/day, conduction losses across the thermal-cylinder boundary and partial drift of the warm volume away from the well reduce recoverable heat to approximately 6229 MWh, corresponding to a seasonal recovery efficiency of approximately 61%, the highest of the three pathways at this velocity. Across the $v_{gw} = 0.02$–0.30 m/day sweep, recovery efficiency ranges from approximately 71% at very low groundwater flow to approximately 50% at the high end, with recovered heat decreasing from approximately 7200 to 5140 MWh.

Overall, the three pathways display distinct annual energy-flow signatures. At the baseline groundwater velocity, ATES provides the largest recoverable energy, closely followed by BTES; both deliver high-quality seasonal heat compensation. The H_2 pathway offers high flexibility on the electrical side but suffers from substantially larger conversion losses across the electrolysis–storage–fuel-cell chain. ATES performance is, however, highly dependent on the assumed groundwater velocity: at higher flow rates (≥ 0.25 m/day) ATES recovery drops below BTES, making BTES the more robust choice in hydrogeologically unfavourable settings.

3.3. Cost and emission outcomes

Cost and emission outcomes are evaluated after the energy results because the economic and carbon rankings depend on both annualised investment and useful winter energy recovery. Fig. 11 shows monthly net costs of each pathway under the PV baseline. The no-PV baseline exhibits a stable cost profile, while the PV baseline maintains near-zero

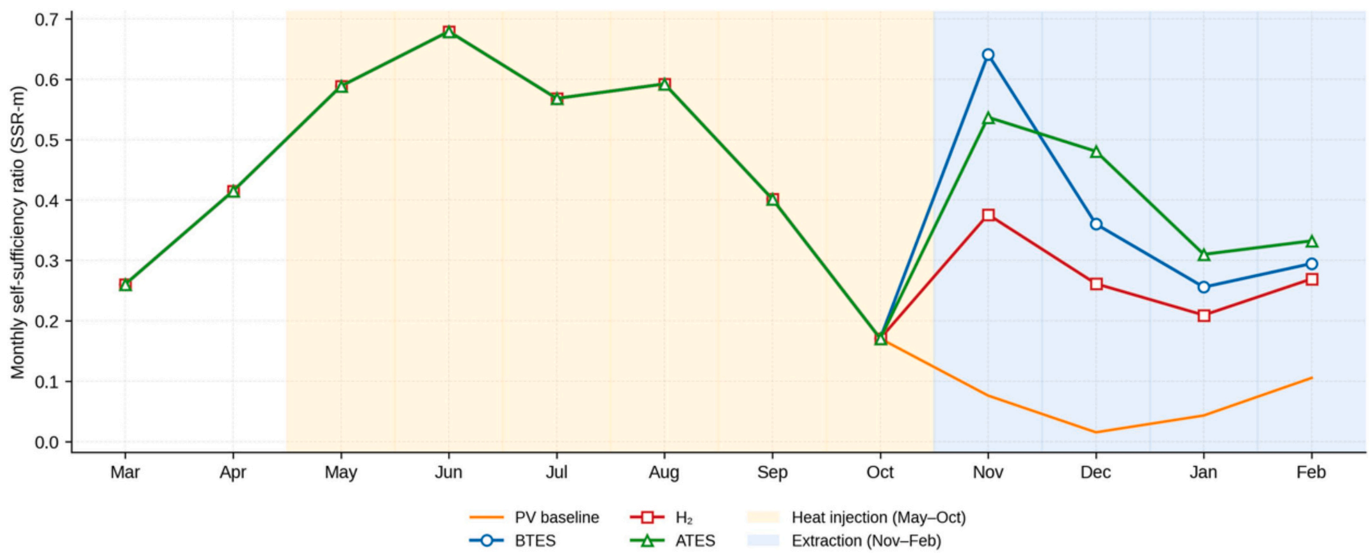

Fig. 8. Monthly self-sufficiency ratios under the three pathways.

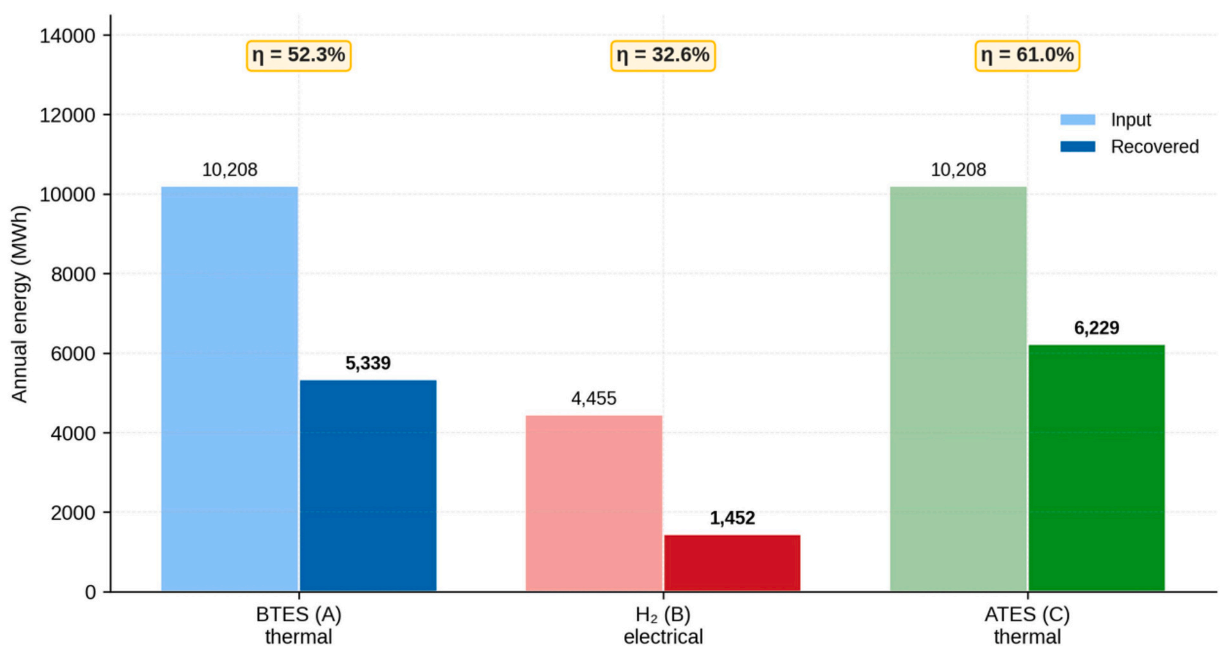

Fig. 9. Input and output energy or electricity for the three technologies (native units: MWh-thermal for BTES/ATES, MWh-electrical for H_2).

net cost for much of the year and rises slightly in winter.

During summer charging, all three pathways have monthly net costs close to the PV baseline because charging is driven by surplus PV. The pathways diverge during winter recovery. Hydrogen has by far the largest net cost, close to 390 k€/month in the discharge period, because its savings do not offset high annualised CAPEX and conversion losses. BTES has the lowest net-cost range, about 12–29 k€/month, while ATES remains moderate, about 62–73 k€/month.

In contrast, BTES and ATES exhibit far smaller net costs. BTES net cost ranges from about 12 to 29 k€/month, while ATES ranges from 62 to 73 k€/month. The BTES range is the closest to break-even of the three pathways, since its monthly savings (28 k€ in November falling to 11 k€ in February) almost cover its monthly amortisation. ATES net cost is moderate and stable, reflecting larger savings paired with a higher CAPEX. The rank order between BTES and ATES varies by month depending on monthly recovery.

Fig. 12 compares winter cost savings and annualised costs. BTES and ATES both reduce winter electricity purchases, with portfolio-level monthly savings of about 11–29 k€/month for BTES and 15–26 k€/month for ATES. Hydrogen savings are smaller, about 10–13 k€/month, and remain far below its annualised cost. The winter decline in savings mainly reflects the monthly reduction in discharge-side COP defined in Eq. (18).

All three pathways show decreasing savings from November to February, driven mainly by the monthly degradation of the discharge-side COP defined in Eq. (18). As the storage cools through winter the COP falls toward its floor (1.6 for BTES, 1.7 for ATES), each kWh of recovered heat displaces fewer kWh of grid electricity. Reduced PV self-consumption in deep winter contributes a smaller share to this trend. This aligns with the observed winter decline in Import-m and SSR-m.

BTES achieves the most favourable energy-cost balance in this case, combining substantial winter recovery with moderate annualised costs.

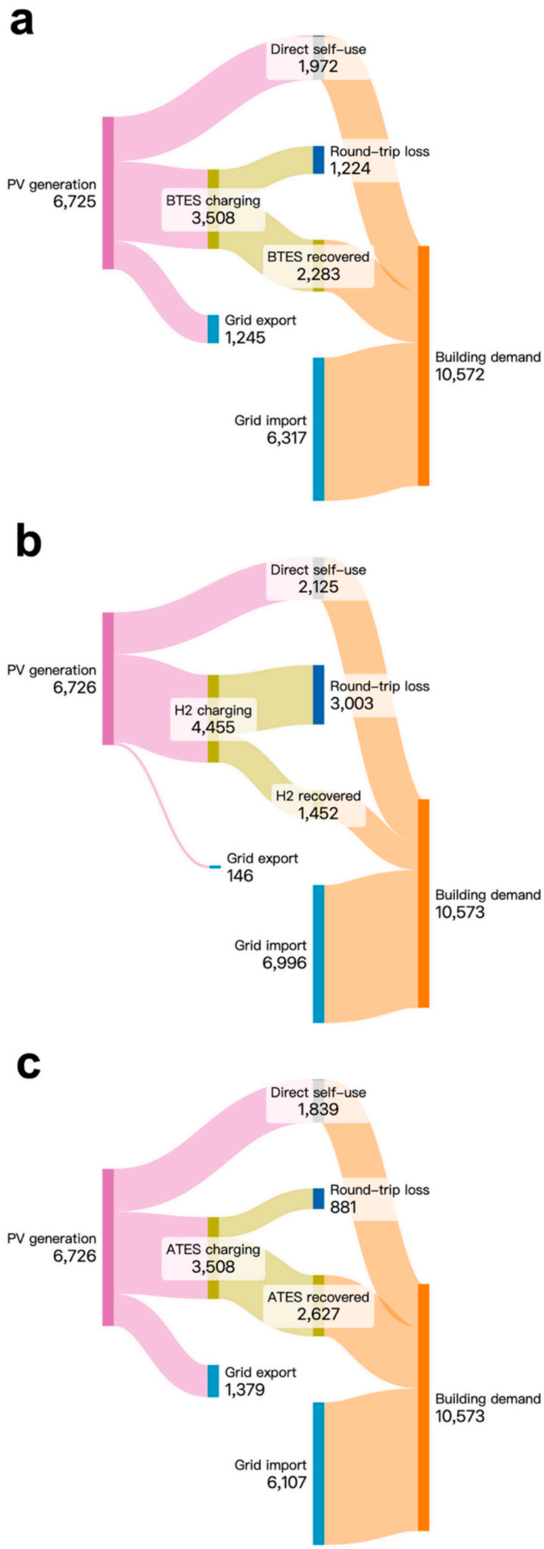

Fig. 10. Sankey diagrams of energy flows for the three seasonal storage technologies (all flows in MWh-electrical equivalent; for BTES/ATES the heat-pump COPs map between thermal storage and electrical input/output).

ATES provides high recovery under the baseline hydrogeological assumption, but its net cost remains higher than BTES because of the assumed component costs and its dependence on aquifer conditions. The hydrogen pathway has the lowest recovered energy and the highest annualised cost, producing the largest winter net cost. The ranking should therefore be interpreted within the selected cost assumptions and the heating-dominated load profile rather than as a universal technology ranking.

The same framework is then used to assess decarbonisation outcomes under three carbon-intensity scenarios: high (0.50 tCO_2/MWh), medium (0.25 tCO_2/MWh), and low (0.05 tCO_2/MWh). Fig. 13 shows the relationship between annual emission reductions and annualised system cost for the 44 buildings. Higher carbon-intensity values yield greater emission-reduction benefits per unit of energy shifted, while decreasing carbon intensity rapidly reduces the direct carbon benefit.

In the high-carbon scenario, BTES and ATES achieve up to 85 (BTES) and 110 (ATES) tCO_2/year of reductions for the largest-consumption buildings, with most buildings clustered below 50 tCO_2/year. The hydrogen pathway reaches up to $\approx$ 57 tCO_2/year and is associated with the highest annualised cost, with some buildings exceeding 350 k€/year. This highlights the strong cost sensitivity of the hydrogen system compared with the two thermal-storage options. BTES and ATES show much more compact distributions, with most buildings achieving non-trivial reductions at annualised costs below 50 k€/year. Bubble size correlates positively with emission-reduction potential, indicating that high-consumption buildings gain the greatest benefits when carbon intensity is high.

Under the medium-carbon scenario, overall emission reductions decrease to 11–55 tCO_2/year. BTES and ATES remain tightly clustered, showing stable performance, while hydrogen continues to occupy the high-cost region. BTES displays a slightly better cost–reduction balance, and ATES shows the most stable behaviour among medium-consumption buildings. These patterns suggest that aquifer heat storage retains meaningful decarbonisation value even as electricity becomes cleaner.

In the low-carbon scenario, all technologies show substantial declines in emission reductions, with most buildings falling in the 0–11 tCO_2/year range. This indicates that in low-carbon power systems, the primary value of seasonal storage shifts away from emission reduction toward peak shaving, self-sufficiency, and energy-system resilience. Hydrogen storage provides almost no meaningful emission reduction in this scenario. BTES and ATES retain small but visible reductions, but their bubble clusters lie close to the horizontal axis, showing that carbon savings are no longer the main driver for deployment.

Overall, the emission results show that carbon intensity is the dominant external driver of decarbonisation value. BTES and ATES provide the most favourable cost-benefit trade-off in high-carbon contexts, while hydrogen loses most of its mitigation advantage as electricity decarbonises. High-load buildings deliver the largest absolute savings and are therefore more suitable priority targets for seasonal-storage deployment.

3.4. Building suitability and sensitivity-based selection boundary

Building-type suitability and sensitivity results identify where seasonal storage is most relevant. Principal component analysis (PCA) was applied to seven variables describing physical scale, age, energy quality, cost, CO_2 reduction, and grid-import reduction (Fig. 14). Features were standardised before decomposition, and building function was used only as a label. The first two components explain 65.8% of total variance. PC1 mainly separates large high-load institutional buildings from small ones, while PC2 reflects construction year and energy-performance label. Bubble area represents heated floor area, and background shading indicates the best CO_2-reduction rate across the three pathways.

Kindergartens cluster in the low-PC1 region, with small floor areas, lower consumption, and limited storage-retrofit benefit. Schools and nursing homes are more dispersed and extend into higher-PC1 regions, reflecting larger loads, more variable demand, and greater technical potential. Office buildings are few and show intermediate behaviour.

The PCA shading highlights a clear deployment hierarchy. High-load buildings in the upper-right region achieve the largest reductions,

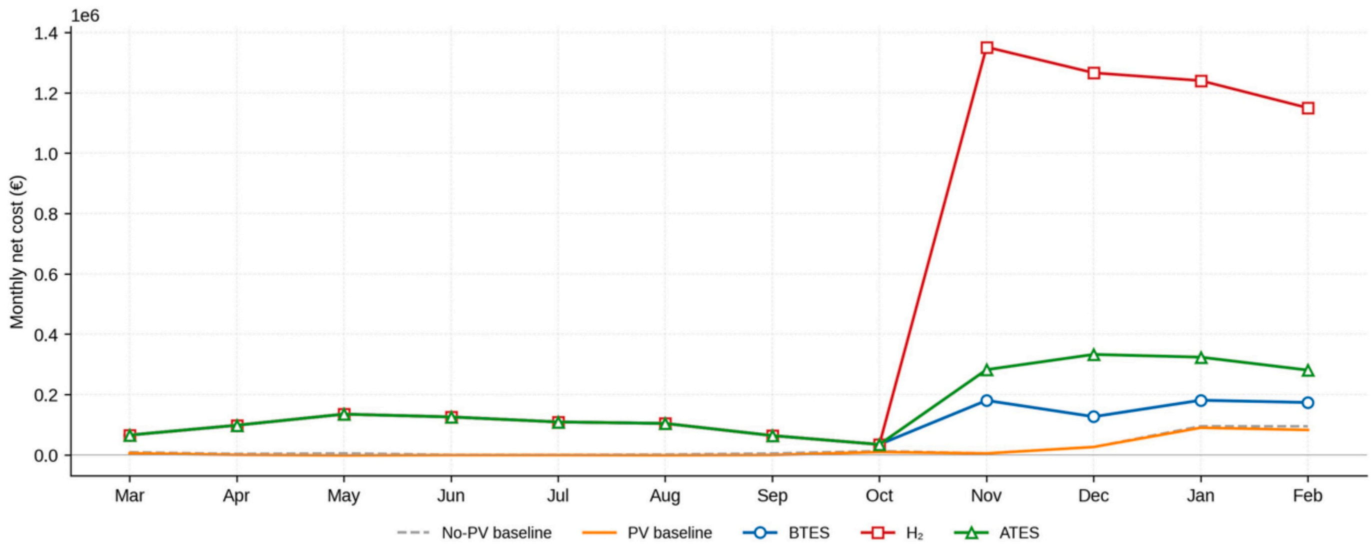

Fig. 11. Monthly net cost of seasonal storage pathways during charging and discharging periods.

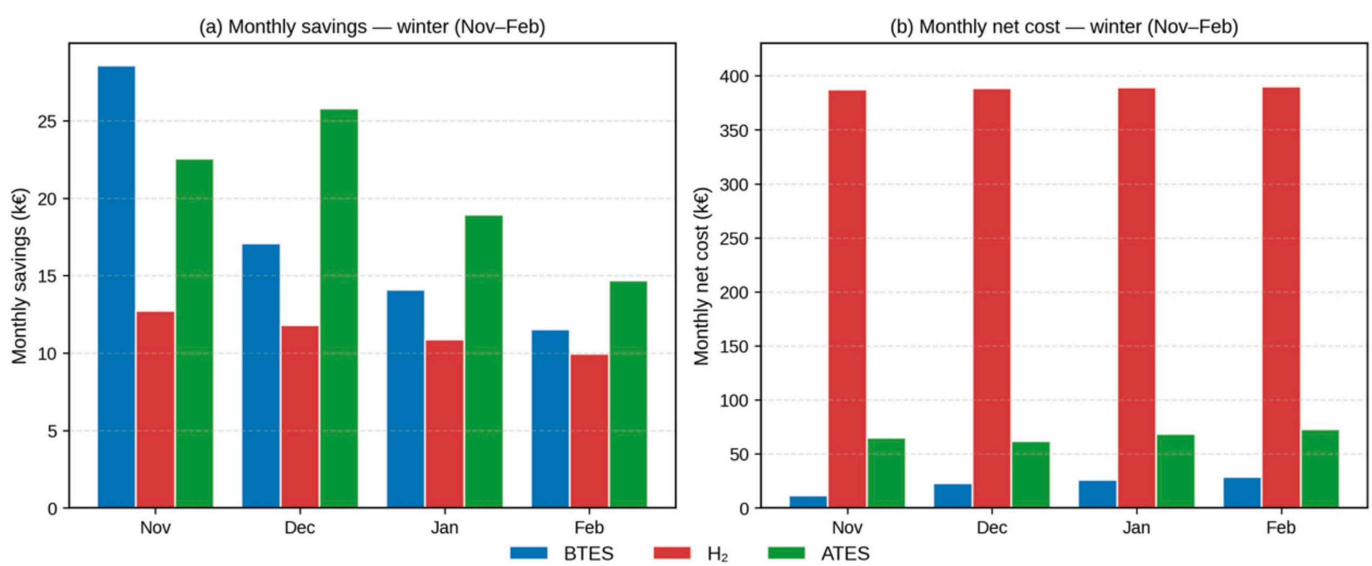

Fig. 12. Winter (November to February) monthly savings (a) and monthly net cost (b) for the three storage pathways. Net cost is defined as the monthly storage CAPEX amortisation (annual cost / 12) minus the monthly savings. Values are portfolio-level totals across the 44 buildings.

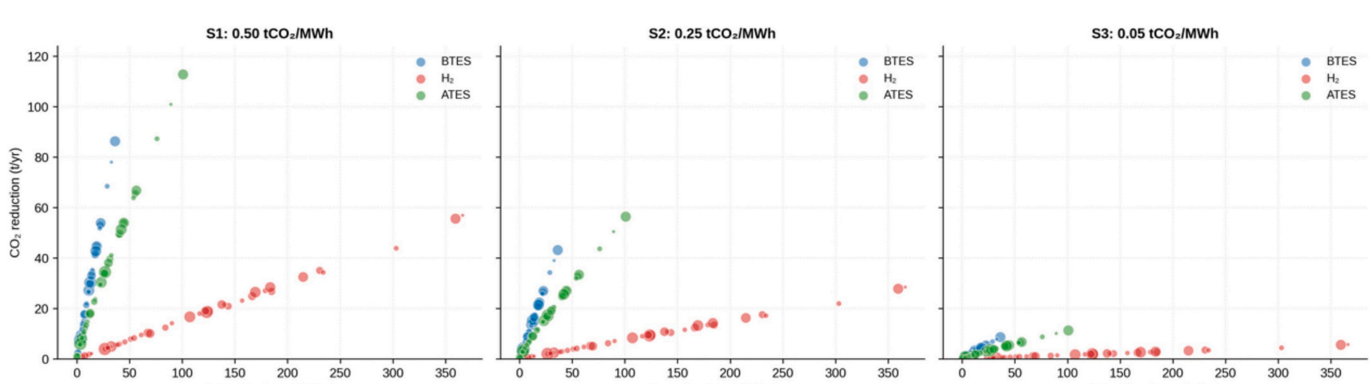

Fig. 13. Retrofitting potential under three electricity carbon-intensity scenarios.

including more than 80 tCO_2/year for the best pathway, whereas small low-load buildings show near-zero potential. This supports prioritising high-consumption, high-occupancy public buildings rather than distributing storage investments evenly across the full building stock.

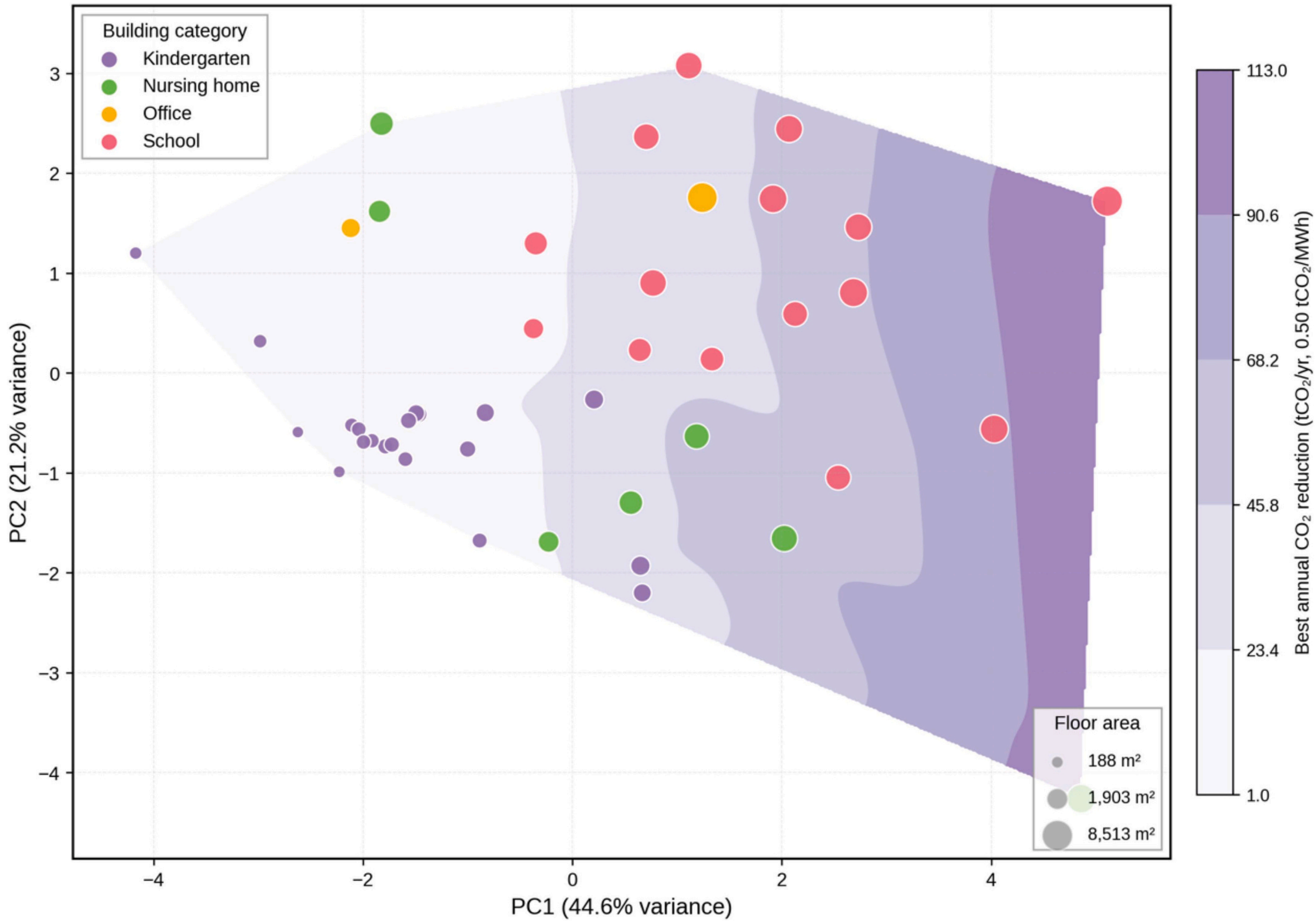

Fig. 14. PCA-based building clustering, with contour shading showing the maximum achievable CO_2-reduction potential across pathways.

Fig. 15 extends the suitability analysis by showing unit delivered-energy cost sensitivity for BTES, hydrogen, and ATES. Baseline costs are 0.226, 3.349, and 0.359 EUR/kWh-el delivered, respectively. The ±10% and ±20% perturbations cover realistic site-to-site variability reported for hard-rock BTES and shallow LT-ATES recovery [9,15,54].

BTES shows the smallest absolute variation, with ±20% perturbations producing cost shifts of −0.038 to +0.056 EUR/kWh-el. Its cost is most sensitive to round-trip efficiency, then CAPEX, with very small price sensitivity. Round-trip efficiency exhibits the strongest sensitivity. A 20% increase reduces cost by ≈ 0.038 EUR/kWh-el, while a 20% decrease increases cost by about 0.030. Electricity-price responsiveness is minimal (±0.003), reflecting BTES's dependence on heat-pump operation and subsurface thermal storage, with a high share of discounted CAPEX and low price elasticity.

Hydrogen shows the strongest sensitivity. Unit cost varies by −0.56 to +0.84 EUR/kWh-el under a ±20% efficiency perturbation and by about ±0.66 EUR/kWh-el under a ±20% CAPEX perturbation. Electricity-price sensitivity is small under the low Nord Pool 2020–2021

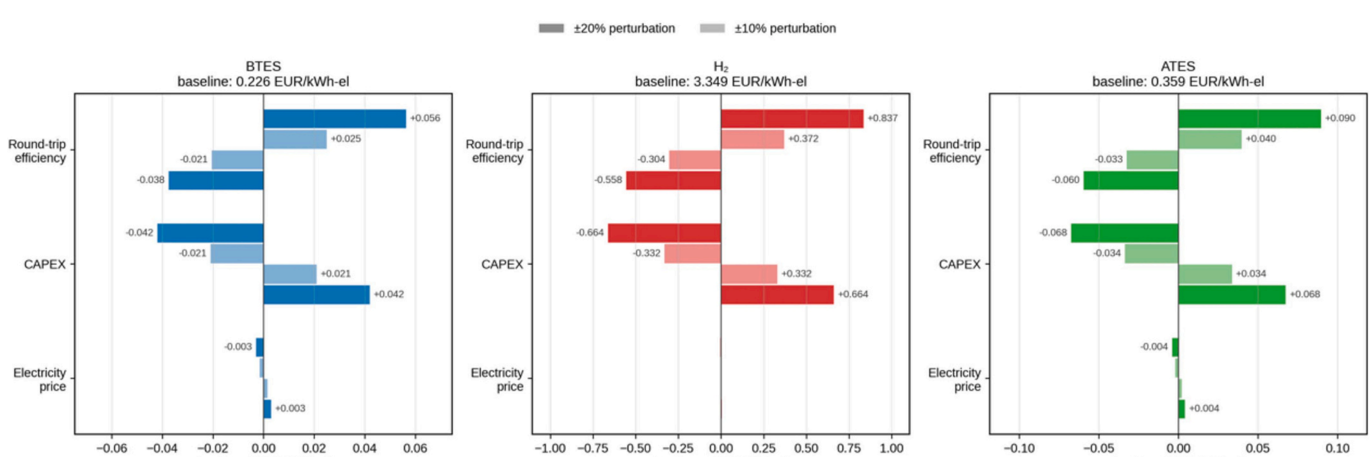

Fig. 15. Sensitivity analysis results.

export prices used here. These results indicate that the hydrogen pathway is dominated by device efficiency and capital cost.

ATES sensitivity lies between BTES and hydrogen, with overall variation within approximately −0.06 to +0.09 EUR/kWh-el under ±20% perturbations. It shows modest linear responses to electricity price, storage CAPEX, and PV CAPEX. Round-trip efficiency again is the strongest driver. A 20% increase reduces cost by about 0.060 EUR/kWh-th, while a 20% decline increases it by about 0.090 EUR/kWh-el. Impacts from electricity price and CAPEX changes are much smaller than those for hydrogen. Despite hydrodynamic losses in the aquifer, ATES maintains a balanced cost structure with no single parameter dominating its behaviour.

Overall, the sensitivity analysis defines the main technology-selection boundary. BTES is the most stable and least sensitive to parameter fluctuations; hydrogen is the most elastic because efficiency and CAPEX dominate its cost; and ATES occupies a middle ground. The key boundary is hydrogeological: ATES can outperform BTES under low-flow aquifer conditions, but at higher groundwater-flow velocities its recovery falls below BTES, making BTES the more robust thermal option when subsurface conditions are uncertain or unfavourable.

4. Discussion

4.1. Comparative interpretation and technology-selection boundary

4.1.1. BTES as the robust thermal-storage option

BTES achieves about 52% seasonal recovery, the second-highest value under the baseline ATES groundwater-flow assumption. Existing cold-climate BTES demonstrations, including Drake Landing, provide useful context for feasibility [7,9,55], but they are not direct performance benchmarks because recovery depends on scale, charging source, borehole configuration, ground properties, operating history, climate, and control strategy. Within the present unified framework, BTES delivers more useful seasonal energy than hydrogen and remains competitive with ATES when aquifer conditions are less favourable. Sensitivity analysis indicates that the unit cost of heat from BTES is the least responsive to parameter changes, far lower than the strong variability observed for hydrogen. This is partly because BTES operation relies mainly on heat pumps and subsurface storage, with a short conversion chain and relatively low losses. It is also due to the cost structure being dominated by upfront drilling and borehole installation rather than operating costs, making BTES less sensitive to energy prices and efficiency variations. Previous work has also reported that in two real building-heating projects, BTES solutions achieved significantly better economics than conventional water-tank storage, with heat costs around one third of the latter [56]. BTES is also adaptable across carbon-intensity scenarios and building types. High-consumption buildings with pronounced winter peaks, especially nursing homes and schools in this dataset, gain the greatest import reductions and emission benefits. These findings support BTES as a robust thermal-storage option for cold-climate public-building clusters, while still requiring local design optimisation of borehole spacing, field size, drilling costs, and heat-pump operation.

4.1.2. Hydrogen as a flexible but costly electricity-side pathway

The hydrogen pathway reaches an annual round-trip efficiency of about 33%, lower than both thermal-storage options in this heating-dominated case. Its main advantage is the recovered energy form: surplus summer renewable electricity is converted to hydrogen and later reconverted to electricity, which can support winter electrical loads directly [15,57]. The results confirm that hydrogen provides winter import reductions with a smoother monthly profile than the thermal pathways because of the imposed discharge schedule. These benefits come at high cost. Hydrogen annualised costs far exceed those of BTES and ATES because of high capital investment and conversion losses across electrolysis, storage, and fuel-cell generation. This is consistent with studies showing that low round-trip efficiency keeps the levelised cost of hydrogen-based electricity high even when component costs decline [25]. Sensitivity analysis confirms that hydrogen economics remain highly dependent on efficiency and CAPEX. The viability of hydrogen storage therefore depends on external conditions that are not guaranteed in the present case, including very low-cost surplus electricity, lower electrolyser and fuel-cell costs, higher carbon prices, or system needs for long-duration electrical flexibility. Under high-carbon electricity, hydrogen still provides noticeable emission reductions, but under low-carbon conditions its mitigation value is small. The results support a cautious interpretation: hydrogen can be a strategic complement for electrical-side seasonal balancing, but it is not cost-competitive with BTES or ATES for the heating-dominated public-building cluster under the assumed efficiencies and costs.

4.1.3. ATES as a high-potential option

Under the baseline ambient groundwater-flow velocity used in this study ($v_{gw} = 0.15$ m/day), ATES achieves a seasonal recovery efficiency of about 61%, the highest of the three pathways. This value lies within the 40–85% range reported for shallow low-temperature ATES systems [58]. Across the v_{gw} sweep from 0.02 to 0.30 m/day, recovery varies from approximately 71% to 50%, illustrating that ATES performance is controlled strongly by local hydrogeology. At groundwater-flow velocities above approximately 0.25 m/day, ATES recovery falls below BTES, making BTES the more robust choice under unfavourable flow conditions. ATES can therefore be the preferred pathway where a suitable confined, low-flow aquifer is available, but it requires stronger site verification than BTES. ATES shows additional advantages in our results. Its winter recovery curve is smoother than that of BTES, with relatively strong contributions across the whole discharge season, and it competes with or exceeds BTES recovery in December–February under baseline groundwater conditions. ATES winter net-cost increase is comparable to BTES and well below H_2. Sensitivity analysis shows moderate unit-cost variability within −0.06 to +0.09 €/kWh-el under ±20% perturbations, slightly higher than BTES but far lower than hydrogen. This indicates that despite hydrodynamic heat losses, ATES is not dominated by a single cost driver and exhibits good economic robustness. ATES falls between BTES and hydrogen in scenario dependence. It can provide large emission reductions where load is high and aquifer conditions are suitable, but its feasibility is limited by hydrogeology and regulation. Its established deployment in offices, commercial buildings, and large building clusters supports its relevance for low- to medium-temperature applications [11,59].

4.1.4. Cost sensitivity and Nordic geological boundary conditions

The preceding analysis highlights a clear stratification in cost sensitivity across the three pathways. BTES is the most robust, hydrogen the most sensitive, and ATES lies in between. BTES relies on mature borehole and heat-pump technology. Its cost structure is dominated by upfront capital expenditure, while operating costs are relatively low. As a result, annualised costs are driven mainly by discounted CAPEX. When electricity prices, efficiencies, or discount rates change, BTES costs shift only slightly. Across multiple perturbation scenarios, unit heat cost changes by less than ±0.06 €/kWh-el under ±20% perturbations.

The hydrogen chain differs because several capital- and efficiency-critical components act in series. Electrolysers, storage tanks, and fuel cells can each become cost bottlenecks, and small changes in stage efficiency affect the overall round-trip efficiency. Literature therefore emphasises advanced electrolysis and fuel-cell improvements when discussing hydrogen economics [25,60]. In the present case, economic feasibility would require much lower-cost surplus electricity, lower component costs, or additional value from long-duration electrical flexibility.

ATES shows moderate cost sensitivity. Drilling and surface-plant investments are relatively modest, and there are no electricity–hydrogen conversion losses. Unit heat-storage cost is mainly affected by subsurface heat losses and heat-pump COP. Previous studies note that site thermal conductivity and groundwater velocity influence storage efficiency, but that optimising borefield layout and increasing storage size can mitigate low initial performance [27]. Our results show that improving ATES round-trip efficiency by 20% reduces unit cost by about 0.06 €/kWh-el, while efficiency losses increase costs but remain far below the shifts observed for hydrogen.

In summary, the economic interpretation reinforces the physical one. BTES is the most robust option under uncertain subsurface and cost conditions, hydrogen is the most volatile and condition-dependent, and ATES can be highly attractive when hydrogeology supports stable recovery. The technology-selection boundary is therefore not defined by recovery efficiency alone, but by the combined effect of local subsurface conditions, delivered-energy cost, and the form of energy needed in winter.

The strong performance of BTES in Nordic contexts is closely tied to regional geological conditions. The Fennoscandian Shield is dominated by crystalline rocks such as granite and gneiss with high thermal conductivity, typically 2.6–4.0 W/m·K, whereas common sedimentary rocks such as sandstone and mudstone in central Europe generally range from 1.3 to 2.0 W/m·K [61–63]. High conductivity facilitates summer heat diffusion away from boreholes, increasing the effective storage volume. It also supports higher heat fluxes at the borehole wall during discharge, improving round-trip efficiency.

In addition, Nordic bedrock tends to have very low permeability (10^{-18}–10^{-20} m^2) and low porosity (<1–3%), leading to weak horizontal groundwater flow [64]. This low-flow environment significantly reduces thermal-front migration, keeping seasonal heat losses much lower than in permeable sedimentary aquifers. For example, monitoring at the Arlanda BTES system in Sweden has shown that BTES in crystalline rock can achieve seasonal recovery efficiencies of about 45–60%, while comparable systems in high-permeability sandstone often fall to 30–35% [54,65].

Finnish case studies similarly identify low permeability and low groundwater velocities as key enablers of efficient BTES operation [66]. In Nordic hard-rock settings, BTES benefits from favourable rock properties and mature drilling practice. ATES can still be attractive where confined sand-gravel aquifers are available, but if such aquifers are absent or groundwater flow is high, BTES remains the more robust default [66].

For typical Nordic hard-rock cities, BTES therefore emerges as the more robust option for seasonal summer-surplus-to-winter-heating cycles. ATES becomes preferable only where a suitable confined low-flow aquifer is available and regulatory constraints allow operation. Hydrogen is best interpreted as a complementary electrical-flexibility option rather than a direct competitor to thermal storage for heating-dominated buildings. This conditional interpretation is central to applying the results beyond the Drammen case study.

4.2. Scenario and deployment implications

As power systems decarbonise, the emission-reduction value of seasonal storage becomes highly scenario-dependent. The three carbon-intensity scenarios in this study (high, medium, low) make this dependence explicit. When grid carbon intensity is high (for example, 0.50 tCO_2/MWh), seasonal storage can substantially reduce grid electricity imports, leading to significant emission reductions. Once electricity supply becomes much cleaner (for example, 0.05 tCO_2/MWh), seasonal storage still reduces purchases from the grid, but the associated CO_2 savings become marginal.

In the high-carbon scenario, BTES and ATES achieve annual CO_2 reductions of about 40–120 t/year for most buildings, while the hydrogen pathway reaches up to roughly 57 t/year in some high-consumption cases. However, these high hydrogen-related reductions are accompanied by the highest annualised costs. Under medium-carbon conditions, reductions for all technologies drop to about 20–60 t/year. BTES and ATES still maintain compact and stable cost–benefit distributions, whereas the high-cost disadvantage of hydrogen becomes more pronounced. Under low-carbon conditions, most buildings achieve less than 10 t/year of reductions, hydrogen loses almost all emission-reduction relevance, and BTES and ATES clusters shift close to the zero axis.

This trend confirms the decisive role of policy context and power-system structure in shaping the mitigation value of storage. When fossil generation still represents a substantial share of electricity supply, seasonal storage can deliver important emission reductions by displacing carbon-intensive peak power. Once the grid becomes near-carbon-neutral, the main value of storage shifts away from direct mitigation toward peak shaving, self-sufficiency, and system reliability. Strategic energy models have reached similar conclusions, arguing that in highly renewable systems, the primary role of long-duration storage is to balance seasonal supply–demand mismatches and avoid curtailment of surplus renewables.

For deeply decarbonised regions such as the Nordic countries, evaluating seasonal storage will therefore require a broader set of metrics, including peak-load reduction, local renewable utilisation, and supply security. From a policy perspective, our results suggest that support schemes should be adaptive. At higher carbon intensities, incentives should prioritise immediately effective thermal-storage options such as BTES and ATES. As grid carbon intensity declines, policy priorities may shift toward valuing the flexibility and resilience contributions of storage rather than its direct CO_2 savings.

Different types of public buildings exhibit distinct load characteristics and levels of compatibility with seasonal storage. Our PCA-based analysis shows that small, low-load buildings such as kindergartens have low energy intensity and modest seasonal variability in heat demand. For these buildings, seasonal storage delivers limited improvements in energy self-sufficiency and modest emission reductions.

In contrast, nursing homes and schools have much higher annual consumption and pronounced winter peaks. Seasonal storage offers significantly higher returns in these cases, reflected in stronger peak-load reduction and larger CO_2 savings. BTES and ATES systems are often deployed first in large buildings or building clusters to exploit economies of scale. Larger buildings provide more opportunities for waste-heat recovery and local utilisation, which helps to spread fixed storage costs more effectively [56].

Temperature requirements also influence suitability. ATES is well suited to low-temperature heating and cooling where a suitable aquifer exists, while BTES can be more appropriate for buildings with stricter heating requirements. The clustering results indicate that high-consumption, high-usage-intensity buildings should be prioritised for demonstration, whereas small low-load buildings may benefit more from envelope retrofits and other efficiency measures.

4.3. Limitations

All three pathways are represented with reduced-order models. The BTES unit-cell model omits three-dimensional end effects and field-edge boundary conditions. The ATES lumped thermal-cylinder model treats groundwater flow parametrically and omits well-to-well interference, aquifer heterogeneity, thermal retardation, and density-driven mixing. The hydrogen chain uses fixed component efficiencies and does not model part-load operation, degradation, or detailed compression electricity. Fully resolved hydrogeological and device-level simulations are left to future work.

Capital cost and lifetime values are drawn from international techno-economic benchmarks (IRENA, IEA, Fraunhofer ISE) and have not been corrected for Norwegian-specific drilling, well-completion, or grid-connection premiums, which can raise installed BTES and ATES costs by 20–50% relative to central European values. A common 7% discount rate is applied to all three technologies for comparability, and storage CAPEX is assumed to scale linearly with inventory. Cluster-scale economies of scale, shared infrastructure, and learning-curve effects on hydrogen components are therefore not explicitly represented. The cost comparison should be read as a relative ranking under unified assumptions rather than an absolute procurement estimate.

The simulation covers one climatic year, March 2020 to February 2021, so inter-annual variability is not assessed. Loads are held identical across storage scenarios, and demand-response interactions are not modelled. Electricity prices follow Nord Pool 2020–2021 quotations, and carbon-intensity scenarios are static rather than dynamic decarbonisation pathways. Storage components are sized per building without modelling physical distance, shared infrastructure, or distribution-network cost. These issues should be included before extending the per-building results to full cluster-scale investment decisions.

5. Conclusions

This study compared BTES, ATES, and a power-to-hydrogen-to-power pathway for the same 44-building public-building cluster in Drammen using a unified hourly energy-balance, cost, and emission framework. The main conclusions are as follows.

(1) The case shows a clear seasonal mismatch: summer PV surplus is available when building demand is low, while the largest electricity and heating-related loads occur in winter. Under the model assumptions, BTES recovers about 5339 MWh from 10,208 MWh of seasonal heat charging (about 52%), ATES recovers about 6229 MWh from the same thermal input at $v_{gw} = 0.15$ m/day (about 61%), and the hydrogen pathway recovers about 1452 MWh of electricity from 4455 MWh used for electrolysis (about 33%).

(2) The economic comparison favours thermal storage for this heating-dominated case. BTES has the most stable cost performance under parameter perturbations, while ATES can provide higher recovery where aquifer conditions are favourable. Hydrogen remains the most expensive pathway under the assumed efficiencies and component costs, although it retains value as an electrical-flexibility option.

(3) Emission benefits depend strongly on grid carbon intensity. Under high-carbon electricity, the largest buildings achieve the highest reductions, reaching up to about 85 tCO_2/year for BTES and 110 tCO_2/year for ATES. Under low-carbon electricity, direct CO_2 reductions become small, so the value of seasonal storage shifts toward peak reduction, renewable self-consumption, and resilience.

(4) Building type affects deployment priority. Nursing homes and schools, with higher loads and stronger winter peaks, are better candidates for seasonal storage than small low-load buildings such as kindergartens. This supports a tiered deployment strategy rather than uniform retrofitting across all public buildings.

(5) Technology selection should remain conditional. BTES is the more robust default where subsurface conditions are uncertain or hard-rock conditions dominate. ATES is preferable where a confined low-flow aquifer is available and permitted. Hydrogen is best treated as a complementary route for long-duration electrical balancing. Future work should add site-calibrated hydrogeology, inter-annual climate variability, and shared-infrastructure costs.

Funding information

This work was supported by the Research Council of Finland (Sustain School Grant No. 359189 and DISCAS, Grant No. 362751), EU Interreg Aurora programme: RESILIFY (project number: 20366468) and EU Cetp programme: NewHeatIntegrated (project number: Cetp-2022-00139).

CRediT authorship contribution statement

Lianghan Cong: Writing – original draft, Methodology, Formal analysis, Conceptualization. **Xiaoshu Lü:** Writing – review & editing, Supervision, Funding acquisition. **Shuaiyi Lu:** Writing – review & editing, Formal analysis. **Pan Jiang:** Methodology, Investigation.

Declaration of generative AI and AI-assisted technologies in the writing process

During the preparation of this work, the authors utilized ChatGPT 5.5 to improve the English language presentation. After employing this service, the authors carefully reviewed and revised the content as necessary, and take full responsibility for the content of the published article.

Declaration of competing interest

The authors declare that they have no known competing financial interests or personal relationships that could have appeared to influence the work reported in this paper.

Acknowledgment

The authors sincerely thank the editor and the two anonymous reviewers for their constructive comments and valuable suggestions, which helped improve the clarity, organization, and overall quality of the manuscript.

Data availability

The data used in this study were obtained from publicly available sources. Building consumption data are available from the COFACTOR Drammen dataset [32].

References

[1] A.T.D. Perera, K. Soga, Y. Xu, P.S. Nico, T. Hong, Enhancing flexibility for climate change using seasonal energy storage (aquifer thermal energy storage) in distributed energy systems, Appl. Energy 340 (2023) 120957, https://doi.org/10.1016/j.apenergy.2023.120957.
[2] V. Sihvonen, I. Ollila, J. Jaanto, A. Grönman, S. Honkapuro, J. Riikonen, A. Price, Role of power-to-heat and thermal energy storage in decarbonization of district heating, Energy 305 (2024) 132372, https://doi.org/10.1016/j.energy.2024.132372.
[3] K. Sornek, M. Homa, F.M. Frigura-Iliasa, M. Frigura-Iliasa, M. Jankowski, K. Papis-Frączek, J. Katerla, J. Janus, Power-to-heat and seasonal thermal energy storage: pathways toward a low-carbon future for district heating, Energies 18 (2025) 5577, https://doi.org/10.3390/en18215577.
[4] S.K. Shah, L. Aye, B. Rismanchi, Seasonal thermal energy storage system for cold climate zones: a review of recent developments, Renew. Sust. Energ. Rev. 97 (2018) 38–49, https://doi.org/10.1016/j.rser.2018.08.025.
[5] X. Zhao, Y. Li, X. Chen, Y. Yin, Ten differences of seasonal borehole thermal energy storage system from ground-source heat pump system, Energ. Buildings 325 (2024) 114994, https://doi.org/10.1016/j.enbuild.2024.114994.
[6] D. Hiris, M.C. Balan, F.I. Bode, A comprehensive review on enhancing seasonal energy storage systems through energy efficiency perspectives, Processes 12 (2024) 1623, https://doi.org/10.3390/pr12081623.
[7] K. Borko, M. Brenčič, Z. Savšek, J. Knez, A. Vozelj, G. Kisel, N. Rman, Insights into aquifer and borehole thermal energy storage systems for Slovenia's energy transition, Energies 18 (2025) 1019, https://doi.org/10.3390/en18051019.
[8] C. Chen, H. Shao, D. Naumov, Y. Kong, K. Tu, O. Kolditz, Numerical investigation on the performance, sustainability, and efficiency of the deep borehole heat exchanger system for building heating, Geotherm. Energy 7 (2019) 18, https://doi.org/10.1186/s40517-019-0133-8.
[9] K.H. Kvalsvik, R.K. Ramstad, H. Holmberg, J. Kocbach, Measurements and simulations of high temperature borehole thermal energy storage in Drammen, Norway - evaluation of thermal losses and thermal barrier, Geothermics 125 (2025) 103192, https://doi.org/10.1016/j.geothermics.2024.103192.
[10] S. Lacombe, E.A. Sudicky, S.K. Frape, A.J.A. Unger, Influence of leaky boreholes on cross-formational groundwater flow and contaminant transport, Water Resour. Res. 31 (1995) 1871–1882, https://doi.org/10.1029/95WR00661.
[11] B. Bourdoncle, Inter-Seasonal Heat Storage in the Residential and Tertiary Sector: A Way to Reduce our Carbon Footprint, Académie des Technologies, Paris, 2020. https://www.academie-technologies.fr/.

[12] R. Stemmle, P. Blum, S. Schüppler, P. Fleuchaus, M. Limoges, P. Bayer, K. Menberg, Environmental impacts of aquifer thermal energy storage (ATES), Renew. Sust. Energ. Rev. 151 (2021) 111560, https://doi.org/10.1016/j.rser.2021.111560.

[13] L. Cong, S. Lu, P. Jiang, T. Zheng, Z. Yu, X. Lü, Research progress on CO2 as geothermal working fluid: a review, Energies 17 (2024) 5415, https://doi.org/10.3390/en17215415.

[14] M. Bonte, B.M. van Breukelen, P.J. Stuyfzand, Temperature-induced impacts on groundwater quality and arsenic mobility in anoxic aquifer sediments used for both drinking water and shallow geothermal energy production, Water Res. 47 (2013) 5088–5100, https://doi.org/10.1016/j.watres.2013.05.049.

[15] G. Fritscher, C. Steindl, J. Helnwein, J. Heger, Hydrogen-enabled microgrids for railway applications: a seasonal energy storage solution for switch-point heating, Sustainability 17 (2025) 8664, https://doi.org/10.3390/su17198664.

[16] H.H.H. Mousa, K. Mahmoud, M. Lehtonen, Multi-timescale coordinated planning of BESS, seasonal hydrogen storage, and dynamic DR for unbalanced RES-rich microgrids, Energy Convers. Manag. 346 (2025) 120510, https://doi.org/10.1016/j.enconman.2025.120510.

[17] L. Li, Y. Sun, Y. Han, W. Chen, Seasonal hydrogen energy storage sizing: two-stage economic-safety optimization for integrated energy systems in northwest China, iScience 27 (2024) 110691, https://doi.org/10.1016/j.isci.2024.110691.

[18] D. Keiner, C. Thoma, D. Bogdanov, C. Breyer, Seasonal hydrogen storage for residential on- and off-grid solar photovoltaics prosumer applications: revolutionary solution or niche market for the energy transition until 2050? Appl. Energy 340 (2023) 121009 https://doi.org/10.1016/j.apenergy.2023.121009.

[19] P. Puranen, A. Kosonen, J. Ahola, Technical feasibility evaluation of a solar PV based off-grid domestic energy system with battery and hydrogen energy storage in northern climates, Sol. Energy 213 (2021) 246–259, https://doi.org/10.1016/j.solener.2020.10.089.

[20] I. Petkov, P. Gabrielli, Power-to-hydrogen as seasonal energy storage: an uncertainty analysis for optimal design of low-carbon multi-energy systems, Appl. Energy 274 (2020) 115197, https://doi.org/10.1016/j.apenergy.2020.115197.

[21] H. ur Rehman, A. Hasan, F. Reda, Challenges in reaching positive energy building level in apartment buildings in the Nordic climate: a techno-economic analysis, Energ. Buildings 262 (2022) 111991, https://doi.org/10.1016/j.enbuild.2022.111991.

[22] M.W. Jack, H.B. Konings, Seasonal variation in electricity demand of solar-powered net-zero energy housing in temperate climates, Energ. Buildings 303 (2024) 113826, https://doi.org/10.1016/j.enbuild.2023.113826.

[23] S. Janke, C. Crawford, A. Truelove, M. Lenio, B. Hashemi, Regenerative hydrogen energy storage modelling for northern microgrid energy design, Renew. Energy 256 (2026) 123979, https://doi.org/10.1016/j.renene.2025.123979.

[24] Y. Cao, Y. Yang, X. Zhao, Q. Li, A review of seasonal hydrogen storage multi-energy systems based on temporal and spatial characteristics, JRM 9 (2021) 1823–1842, https://doi.org/10.32604/jrm.2021.015722.

[25] M. Sayer, A. Ajanovic, R. Haas, Current and future costs of storage for electricity in a decarbonized electricity system, Clean Energy Sustainability 2 (2024) 10012, https://doi.org/10.35534/ces.2024.10012.

[26] D. Tziritas, G.M. Stavrakakis, D. Bakirtzis, G. Kaplanis, K. Patlitzianas, M. Damasiotis, P.L. Zervas, Techno-economic analysis of a hydrogen-based power supply backup system for tertiary sector buildings: a case study in Greece, Sustainability 15 (2023) 7646, https://doi.org/10.3390/su15097646.

[27] T. Yang, W. Liu, G.J. Kramer, Q. Sun, Seasonal thermal energy storage: a techno-economic literature review, Renew. Sust. Energ. Rev. 139 (2021) 110732, https://doi.org/10.1016/j.rser.2021.110732.

[28] S. Schüppler, P. Fleuchaus, P. Blum, Techno-economic and environmental analysis of an aquifer thermal energy storage (ATES) in Germany, Geotherm. Energy 7 (2019) 11, https://doi.org/10.1186/s40517-019-0127-6.

[29] W. Hagemann, J. Weichmann, H. Gernandt, F. Krenzlin, J. Schiffer, Modeling and optimization of borehole thermal energy storage systems using physics-based neural networks, Renew. Energy 256 (2026) 123753, https://doi.org/10.1016/j.renene.2025.123753.

[30] A. Lyden, C.S. Brown, I. Kolo, G. Falcone, D. Friedrich, Seasonal thermal energy storage in smart energy systems: district-level applications and modelling approaches, Renew. Sust. Energ. Rev. 167 (2022) 112760, https://doi.org/10.1016/j.rser.2022.112760.

[31] J. Hirvonen, S. Sirén, P. Sormunen, Seasonal waste heat storage in energy-efficient Finnish apartment buildings, in: M. Kioumarsi, B. Shafei (Eds.), The 1st International Conference on Net-Zero Built Environment, Springer Nature Switzerland, Cham, 2025, pp. 489–498, https://doi.org/10.1007/978-3-031-69626-8_41.

[32] S.K. Lien, H.T. Walnum, Å.L. Sørensen, COFACTOR Drammen dataset - 4 years of hourly energy use data from 45 public buildings in Drammen, Norway, Sci. Data 12 (2025) 393, https://doi.org/10.1038/s41597-025-04708-3.

[33] Nord Pool AS, Day-Ahead Prices. https://data.nordpoolgroup.com/auction/day-ahead/prices, 2026.

[34] P. Eskilson, Thermal Analysis of Heat Extraction Boreholes, Doctoral Thesis (Compilation), 1987.

[35] C. Doughty, G. Hellström, C.F. Tsang, J. Claesson, A dimensionless parameter approach to the thermal behavior of an aquifer thermal energy storage system, Water Resour. Res. 18 (1982) 571–587, https://doi.org/10.1029/WR018i003p00571.

[36] M. Bloemendal, N. Hartog, Analysis of the impact of storage conditions on the thermal recovery efficiency of low-temperature ATES systems, Geothermics 71 (2018) 306–319, https://doi.org/10.1016/j.geothermics.2017.10.009.

[37] Y. Chen, S. Wang, T. Li, Analysis of rooftop photovoltaic potential and electricity planning in Lanzhou urban areas, Buildings 15 (2025) 2207, https://doi.org/10.3390/buildings15132207.

[38] J. Melius, R. Margolis, S. Ong, Estimating Rooftop Suitability for PV: A Review of Methods, Patents, and Validation Techniques, National Renewable Energy Laboratory (NREL), Golden, CO, 2013. https://www.nrel.gov/docs/fy14osti/60593.pdf.

[39] S.E.U. Team, Why are Solar PV Panels Getting Bigger? Solar Energy UK (, 2021. https://solarenergyuk.org/why-are-solar-pv-panels-getting-bigger/ (accessed November 6, 2025).

[40] A. Walker, J. Desai, Understanding Solar Photovoltaic System Performance: An Assessment of 75 Federal Photovoltaic Systems, U.S. Department of Energy, Federal Energy Management Program (FEMP), Golden, CO, 2021. https://www.energy.gov/eere/femp/optimizing-solar-photovoltaic-performance-longevity.

[41] X. Wang, L. Xia, C. Bales, X. Zhang, B. Copertaro, S. Pan, J. Wu, A systematic review of recent air source heat pump (ASHP) systems assisted by solar thermal, photovoltaic and photovoltaic/thermal sources, Renew. Energy 146 (2020) 2472–2487, https://doi.org/10.1016/j.renene.2019.08.096.

[42] E.K. Vakkilainen, Boiler processes, in: Steam Generation from Biomass, Elsevier, 2017, pp. 57–86, https://doi.org/10.1016/B978-0-12-804389-9.00003-4.

[43] J. Pospíšil, M. Špiláček, P. Charvát, Seasonal COP of an air-to-water heat pump when using predictive control preferring power production from renewable sources in the Czech Republic, Energies 12 (2019) 3236, https://doi.org/10.3390/en12173236.

[44] D. Gibb, J. Rosenow, R. Lowes, N.J. Hewitt, Coming in from the cold: heat pump efficiency at low temperatures, Joule 7 (2023) 1939–1942, https://doi.org/10.1016/j.joule.2023.08.005.

[45] N. Catolico, S. Ge, J.S. McCartney, Numerical modeling of a soil-borehole thermal energy storage system, Vadose Zone J. 15 (2016) vzj2015.05.0078, https://doi.org/10.2136/vzj2015.05.0078.

[46] IRENA, Green Hydrogen Cost Reduction: Scaling Up Electrolysers to Meet the 1.5°C Climate Goal, International Renewable Energy Agency, Abu Dhabi, 2020. https://www.irena.org/publications/2020/Dec/Green-hydrogen-cost-reduction.

[47] K. Franzén, Evaluating Electrolyser Setups for Hydrogen Production from Offshore Wind Power : A Case Study in the Baltic Sea. https://urn.kb.se/resolve?urn=urn:nbn:se:kth:diva-336595, 2023.

[48] IEA Hydrogen TCP, Task 42 Hydrogen Storage Report: European Project Database and Cost Summary, IEA Hydrogen TCP, Paris, France, 2023.

[49] D. Feldman, M. Bolinger, P. Schwabe, Current and Future Costs of Renewable Energy Project Finance Across Technologies, 2020, https://doi.org/10.2172/1660124.

[50] S. Philipps, W. Warmuth, J. Rentsch, A. Bett, B. Burger, Photovoltaics Report, Fraunhofer Institute for Solar Energy Systems ISE, Freiburg, Germany, 2025. https://www.ise.fraunhofer.de.

[51] M. Lanahan, P.C. Tabares-Velasco, Seasonal thermal-energy storage: a critical review on BTES systems, modeling, and system design for higher system efficiency, Energies 10 (2017) 743, https://doi.org/10.3390/en10060743.

[52] IEA, Global Hydrogen Review 2023, International Energy Agency, Paris, France, 2023. https://www.iea.org/reports/global-hydrogen-review-2023.

[53] E. Ltd, Fuel Cell Industry Review 2022, E4tech Ltd, London, United Kingdom, 2022. https://www.e4tech.com/reports/fuel-cell-industry-review-2022.php.

[54] E. Nilsson, P. Rohdin, Empirical validation and numerical predictions of an industrial borehole thermal energy storage system, Energies 12 (2019) 2263, https://doi.org/10.3390/en12122263.

[55] H. Karasu, I. Dincer, Life cycle assessment of integrated thermal energy storage systems in buildings: a case study in Canada, Energ. Buildings 217 (2020) 109940, https://doi.org/10.1016/j.enbuild.2020.109940.

[56] A. Hesaraki, S. Holmberg, F. Haghighat, Seasonal thermal energy storage with heat pumps and low temperatures in building projects—a comparative review, Renew. Sust. Energ. Rev. 43 (2015) 1199–1213, https://doi.org/10.1016/j.rser.2014.12.002.

[57] X. Yu, A.M. Abed, M.A. Alghassab, M.N. Khan, F.M. Alhomayani, Z. Chen, J. Tian, One system, three comforts: techno-economic GA-based optimization of a solar power-driven to produce green H2/electricity/cooling/ hot water, Energy 316 (2025) 134560, https://doi.org/10.1016/j.energy.2025.134560.

[58] P. Fleuchaus, B. Godschalk, I. Stober, P. Blum, Worldwide application of aquifer thermal energy storage – a review, Renew. Sust. Energ. Rev. 94 (2018) 861–876, https://doi.org/10.1016/j.rser.2018.06.057.

[59] P. Fleuchaus, S. Schüppler, M. Bloemendal, L. Guglielmetti, O. Opel, P. Blum, Risk analysis of high-temperature aquifer thermal energy storage (HT-ATES), Renew. Sust. Energ. Rev. 133 (2020) 110153, https://doi.org/10.1016/j.rser.2020.110153.

[60] V.G. Sharmila, J.R. Banu, S.-H. Kim, G. Kumar, A review on evaluation of applied pretreatment methods of wastewater towards sustainable H2 generation: energy efficiency analysis, Int. J. Hydrog. Energy 45 (2020) 8329–8345, https://doi.org/10.1016/j.ijhydene.2020.01.081.

[61] J. Claesson, G. Hellström, Multipole method to calculate borehole thermal resistances in a borehole heat exchanger, HVAC&R Res. 17 (2011) 895–911, https://doi.org/10.1080/10789669.2011.609927.

[62] S. Lu, P. Jiang, L. Cong, T. Zheng, Y. Hao, X. Lü, Review of geochemical processes in CCUS: mechanisms, processes, and implications, Gondwana Res. 146 (2025) 200–215, https://doi.org/10.1016/j.gr.2025.05.023.

[63] S. Lu, Z. Yu, Y. Zhang, T. Xu, Review of non-isothermal processes in CCUS from a geomechanical perspective, Earth Sci. Rev. 255 (2024) 104848, https://doi.org/10.1016/j.earscirev.2024.104848.

[64] M.J. Gimeno, E.-L. Tullborg, A.-C. Nilsson, L.F. Auqué, L. Nilsson, Hydrogeochemical characterisation of the groundwater in the crystalline basement of Forsmark, the selected area for the geological nuclear repositories in Sweden, J. Hydrol. 624 (2023) 129818, https://doi.org/10.1016/j.jhydrol.2023.129818.
[65] J. Luo, Y. Shao, Z. Yan, X. Han, Q. Guo, Thermal performance enhancement of borehole heat exchangers by thermally induced groundwater convection in aquifers, Renew. Energy 243 (2025) 122539, https://doi.org/10.1016/j.renene.2025.122539.
[66] J. Keskitalo, Techno-Economic Analysis of Seasonal Thermal Energy Storages in Public Real Estates, Master's Thesis, Lappeenranta-Lahti University of Technology LUT, 2020.